Přírodovědecká fakulta Univerzity Palackého
v Olomouci

Společná laboratoř optiky

Kvantově korelované fotonové páry v moderních fotonických strukturách

DIZERTAČNÍ PRÁCE

Jiří Svozilík

školitel:
doc. RNDr. Jan Peřina ml., Ph.D.

Olomouc 2013

Faculty of Science, Palacký University
in Olomouc

Joint Laboratory of Optics

Entangled photon pairs in modern photonic structures

Ph.D. thesis

Jiří Svozilík

supervisor:
doc. RNDr. Jan Peřina Jr., Ph.D.

Olomouc 2013

Bibliographic details

Title	Entangled photon pairs in modern photonic structures
Nadpis	Kvantově korelované fotonové páry v moderních fotonických strukturách
Type	Ph.D. thesis
Author	Jiří Svozilík
Supervisor	doc. RNDr. Jan Peřina Jr., Ph.D.
University	Palacký University in Olomouc
Study program	P1703 Physics, 1701V029 Optics and Optoelectronics
Department	Joint Laboratory of Optics
Language	English
Year	2013
Pages	74

Statement of originality

I hereby declare that this thesis is my own work and that, to the best of my knowledge and belief, it contains no material previously published or written by another person nor material which to a substantial extent has been accepted for the award of any other degree or diploma of the university or other institute of higher learning, except where due acknowledgement has been made in the text.

In Olomouc, ..., 2013 .....

Submitted on ....., 2013

The author grants permission to Palacký University in Olomouc to store and display this thesis and its electronic version in university library and on official website.

Acknowledgement

I wish to thank, first and foremost, my supervisor Jan Peřina Jr., Ph.D. for his generous support and guidance during my doctoral study. Further, I would like to thank my colleagues Jan Soubusta, Ph.D. and Radek Machulka for their supportive discussions.

My thanks belong to my colleagues and friends Roberto de Jesús León-Montiel, Anaid Rosas, Yannick Alan de Icaza Astiz, Adam Vallés Marí and Martin Hendrych. I am also grateful to prof. J. P. Torres for his encouragement during my stay in ICFO.

Most importantly, my greatest thanks go to my family to whom this dissertation is dedicated.

The author

Contents

Chapter 1

Goals of the Thesis

This work is devoted to the investigation of generation of entangled photon pairs in the nonlinear process of spontaneous parametric down-conversion in modern photonic structures. The thesis is composed of three main parts.

First part of the thesis covers the review of topics of quantum and non-linear optics. In chapter 2, historical and current perspectives on quantum correlations called entanglement are present. Followed by the sections related to the definition of entangled pure states, measures of entanglement and list of applications of entanglement are given. The next chapter 3 is dedicated to fundamentals of nonlinear optics. The transition from classical to quantum descriptions of optical fields is studied by means of the quantization of electromagnetic field. Using a full quantum model, spontaneous parametric down-conversion is described invoking the first order perturbation solution of the Schrödinger equation. Also some quantities needed for randomly poled crystals in chapters 5 and 6 are introduced here. Methods of characterization of temporal features of photon pairs, namely by Hong-Ou-Mandel interference and sum-frequency generation, are described in the last section of this chapter. Chapter 4 is focused on a brief description of techniques of phase-matching of the interacting electromagnetic fields. Natural phase-matching, quasi-phase-matching and stochastic quasi-phase-matching techniques are discussed. We also shortly describe the fabrication process of periodic poling.

Second part of the thesis is devoted to the analytical and numerical studies of properties of photon pairs emitted in randomly poled structures (RPSs). In chapter 5 we investigate the effect of random disturbances in the position of boundaries of ferroelectric domains in a crystal. The random disturbances are considered to have Gaussian probability distributions, which allow us to simplify the analytical model and reach the average values of physical quantities of interest. Photon emission spectra and also

photon-pair generation rates showing a linear dependence on the number of layers regardless of the level of randomness are examined the first. The spectra of photons depend strongly on the amount of randomness in such way, that a higher randomness leads to broader photon spectra. We also show a close relation between random structures and linearly chirped periodically poled structures. This similarity is based on the fact, that both kinds of structures are capable to produce photons with broad bandwidth. This similarity provides transformation curves between the parameter characterizing randomness and that giving the amount of chirping of the ordered linearly chirped poled structures. Both structures can be alternatively compared by considering equal spectral widths or equal numbers of generated photon pairs. Temporal characteristics such as entanglement time for the studied structures decrease with an increase of randomness. Similar behavior is observed in case of correlation time investigated by the sum-frequency generation. Spatial distribution of photon pairs and correlation areas show additional similarities between the random structures and linearly chirped periodically poled structures. We also pay attention to the dependence of spectra on temperature and fabrication induced errors.

The third part of the presented thesis contained in chapter 6 is devoted to the investigation of the higher-multiple orders of the stochastic quasi-phase-matching in randomly poled structures. The analysis of higher orders is motivated by the difficulties of usual poling techniques to create alternated domains of lengths comparable to the needed domains' length μm required by phase-matching the electromagnetic fields of short wavelengths. It is shown that photon-pair rates decrease for higher orders and also for higher amount of randomness. In the spectral domain, the photons exhibit narrower spectra for the third-order phase matching than for the first-order phase matching. This is also reflected in the time domain by longer entanglement times accessible by the Hong-Ou-Mandel interferometry.

The scientific results presented in this thesis are based on the following papers:

- J. Svozilík and J. Peřina Jr., *Intense ultra-broadband down-conversion from randomly poled nonlinear crystals*, Opt. Express **18**, 27130 (2010).
- J. Peřina Jr. and J. Svozilík, *Randomly poled crystals as a source of photon pairs*, Phys. Rev. A **83**, (2011) 033808.
- J. Svozilík and J. Peřina Jr., *Higher-order stochastic quasi-phase-matching in spontaneous parametric down-conversion*, submitted to Optics Communications.

We note that the author has also published several other papers listed on page 65

devoted to photon-pair generation in other photonic structures than nonlinear poled crystals.

Chapter 2

Quantum Entangled States

2.1 Past and Present of Quantum Entanglement

Since its discovery, quantum mechanics (QM) became one of the most successful physical theories, despite that Einstein, Podolsky and Rosen (EPR) had published a controversial paper [1] claiming, that the QM cannot be correct in describing the physical reality. They came up with a "gedanken experiment", in which they admitted that if one has two particles which were allowed to interact at the beginning, then there exists a way how to determine their mutual properties regardless of their mutual spatial separation. Their explanation is demonstrated on a simple example using an electron spin orientation. If one observer measures the first particle with the spin up, then the second observer possessing the second particle measures the spin orientation with the result down and vice versa. This was called "spooky action at a distance". However, Schrödinger figured out, that on the contrary, their idea is a very special inherent feature of quantum mechanics [2]. This phenomenon became later known as entanglement. In the following years, several questions have arisen regarding the possibilities of determining properties of entangled particles in terms of local hidden variables. This issue has been resolved by Bell [3], who has proposed a test of validity of hidden variables theories. Nowadays, the Bell inequality and its derivatives serve as a fundamental test of the presence of entanglement between two quantum systems [4, 5].

For experimental demonstration of validity of quantum mechanics, sources of entangled particles needed to be developed. The first sources of entangled particles (photons) were based on the energy level cascade of Ca atoms, where the radiative transitions permit a direct generation of polarization entangled photon pairs [6, 7]. On the same principle, quantum dots were also shown to be able to emit entangled photon pairs via the

biexciton-radiative decay cascade [8, 9] later. On the other hand, the most commonly used sources of entangled photons are based on the nonlinear optical process of spontaneous parametric down-conversion (SPDC) in optical crystals. In this process, the generated photons can be entangled in many degrees of freedom, such as frequency, momentum, time, polarization and angular orbital momentum [10, 11] [A11]. The emission of entangled photons has been documented by Bouwmeester et al. [12] considering the nonlinear anisotropic optical crystal as a source of photon twins entangled in polarization. Polarization entangled photons were directly harvested in the cross-section point of two emission cones of each polarization. Since photons were collected in a very small area, this kind of source has exhibited a low photon flux. Later, an idea of photon flux enhancement was presented by Kwiat et al. [13] using two mutually-rotated thin nonlinear crystals. Beside that the post-selection based polarization entanglement can also be created from non-entangled photon twins when they are sent on a beam splitter [14]. Advances in semiconductor technologies have allowed the development of integrated photon-pair sources based on the Silica [15] and AlGaAs [16, 17] [A6, A8, A15] waveguides. Additionally, modal entanglement in waveguides has been presented in [18, 19].

2.2 Definition of Entangled Quantum States

Let us consider the Hilbert space $\mathcal{H}_{12} = \mathcal{H}_1 \otimes \mathcal{H}_2$ being composed of two spaces $\mathcal{H}_1$ and $\mathcal{H}_2$ corresponding to two quantum particles. The state of each particle is denoted as $|\Psi\rangle_1$ ($|\Psi\rangle_2$). These two particles are entangled, i.e. in an EPR state, when their global pure state cannot be written in the product form:

$$|\Psi\rangle_{12} \neq |\Psi\rangle_1 |\Psi\rangle_2. \tag{2.1}$$

This definition is valid for the discrete or continuous entanglement. Here we deal solely with the continuous entanglement in frequency, time and space domains. Particularly for the pure states, factorisability of these states can be analysed using the Schmidt decomposition [20, 21]. One can consider a general two-photon state in the form:

$$|\Psi\rangle_{12} = \int dx \int dy \mathcal{A}(x, y) |x\rangle_1 |y\rangle_2, \tag{2.2}$$

where the function $\mathcal{A}(x, y)$ is the probability amplitude of finding the first photon in the state x together with the second one in the state y. The Schmidt decomposition of

this function is expressed as:

$$\mathcal{A}(x,y) = \sum_n \sqrt{\lambda_n} f_n(x) g_n(y), \tag{2.3}$$

where the eigenvalue λ_n and its corresponding eigenfunctions f_n and g_n are obtained as a solution of integral equations:

$$\int dx' K_1(x,x') f_n(x') \quad = \lambda_n f_n(x), \tag{2.4}$$

$$\int dy' K_2(y,y') g_n(y') \quad = \lambda_n g_n(y). \tag{2.5}$$

The integral kernels are defined as:

$$K_1(x,x') \quad = \int dy \mathcal{A}(x,y)\mathcal{A}^*(x',y), \tag{2.6}$$

$$K_2(y,y') \quad = \int dx \mathcal{A}(x,y)\mathcal{A}^*(x,y'). \tag{2.7}$$

We can state after inspecting Eq. (2.3) that the state is entangled when there is more than one nonzero eigenvalue λ_n. From the knowledge of the number of eigenvalues we can calculate the effective amount of contributing modes in the entangled state [21]. This corresponds to the Schmidt number K defined as:

$$K = \frac{1}{\sum_n \lambda_n^2}, \tag{2.8}$$

where $\sum_n \lambda_n = 1$ is assumed. The state is separable if $K = 1$. Entropy of entanglement E [20, 22] can be expressed using the above defined eigenvalues λ_n as:

$$E = -\sum_n \lambda_n \log_2(\lambda_n). \tag{2.9}$$

The state is entangled if E is larger than 0.

2.3 Applications of Entangled States

Quantum dense coding and quantum teleportation are the most representative cases of the use of EPR particles in the area of quantum information transfer. In the case of dense coding, two bits of classical information are send via one bit of quantum information [23]. In this protocol, entangled photon twins are shared between the transmission and receiving stations. In the transmission station, an appropriate local

operation (corresponding to the identity or to one of the Pauli operations) is applied on one particle according to the information being transferred. After, the particle is send to the receiving station, where both entangled particles are combined and information about the applied operation is extracted. Quantum teleportation works in the similar way. This protocol allows to transfer an unknown state of one particle to the second one, as it has been theoretically predicted by Bennett et al. [24] and later also experimentally confirmed by Bouwmeester et al. [12]. This protocol uses EPR particles as a mediator of the information transfer. The particle in initial state, which is going to be teleported, passes via the Bell-state measurement together with one of the entangled particles. Note that in this moment the state of the initial particle is completely destroyed. The result of measurement is then sent via a classical communication channel to the receiving station. A uniform transformation is applied on the second particle of the EPR pair here. That way, the teleportation is accomplished. Necessity of a classical communication channel precludes violation of the special theory of relativity and therefore superluminal transfer is not possible. Also quantum cryptography can take benefits of using EPR photon pairs, as it has been presented in [25], where polarization-entangled photons are sent to two receiving stations. In each station, the measurement of polarization in two orthogonal basis (which are randomly changed) is performed. These two stations reveal their bases for each measurement and separate results to two groups. The first group contains results where the basis were different and these results of measurement are used for testing of violation of the Bell inequality, i.e. if there is no eavesdropper. The second group then contains the results in the same bases and so are used as an encryption key for secured communication.

A large amount of quantum computing algorithms is based on the entanglement [26, 27]. As it has been shown for the first time by David Deutsch [28] the quantum entanglement permits to process a specific group of computing tasks much more faster than the classical computers. Deutsch's algorithm allows to determine if an unknown function is constant for all input cases or not. Classically, one has to try all combinations of the input variables to accomplish this task. Using the quantum entanglement, this task is done in a single step. Famous Shore's algorithm for the factorization of large integral numbers [29] and Grover's searching algorithm [30] [A10] are both also based on the principle of initial entangled state.

In quantum meteorology, EPR states generally allow to enhance the precision of a measurement [31, 32] in comparison with the classical approach of repeated measurements. As an example, the Ramsey spectrometry of ions in the ideal decoherence-free scenario can be considered. Here the entanglement allows to increase the precision of de-

termination of the frequency of atomic transition for n-ions by the factor $\sqrt{n}$ [33]. In the case of quantum optical coherence tomography, the utilization of entangled photon pairs is capable to double the axial resolution of the interferometric measurement together with the dispersion cancellation [34, 35]. Moreover, highly entangled N00N-states offer a way how to increase the resolution bellow the Rayleigh limit in the interferometric setups for an ultra-precise measurement of distances [36].

Chapter 3

Nonlinear Optical Processes as Sources of Entangled Photon Pairs

3.1 Classical Formulation of Nonlinear Optics

Nonlinear interaction of light with atoms of a medium allows to create wavelengths, which even don't occur in the incident light. From the classical point of view, a driven wave-equation:

$$\Delta \mathbf{E} - \frac{1}{c^2}\frac{\partial^2 \mathbf{E}}{\partial t^2} = \frac{1}{c^2}\frac{\partial^2 \mathbf{P}}{\partial t^2} \tag{3.1}$$

derived from the Maxwell equations can be enriched by nonlinear contributions by mean of generalizing the induced polarization $\mathbf{P}$ [37–39]. The induced polarization $\mathbf{P}$ can be expressed as the following series:

$$\mathbf{P}(\mathbf{r},t) = \chi^{(1)} : \mathbf{E}(\mathbf{r},t) + \chi^{(2)} : \mathbf{E}(\mathbf{r},t)\mathbf{E}(\mathbf{r},t) + \chi^{(3)} : \mathbf{E}(\mathbf{r},t)\mathbf{E}(\mathbf{r},t)\mathbf{E}(\mathbf{r},t) + ... \tag{3.2}$$

$\chi^{(1)}$ is the linear optical susceptibility, whereas $\chi^{(2)}$ and $\chi^{(3)}$ are nonlinear optical susceptibilities of the second and third order. The symbol : represents the tensor contracting. The second term on the right side of Eq.(3.2) is responsible for second-order nonlinear effects such as second-harmonic generation, sum- and difference-frequency generation, and also spontaneous parametric down-conversion. Energy-level diagrams of these processes are presented in Fig. 3.1. Virtual levels are marked by the dashed line and E_g stands for the ground energy level of atoms. The third term in Eq. (3.2) includes processes of third-harmonic generation, dependence of the index of refraction on light intensity and other four-waves mixing nonlinear processes.

Let us now examine in detail properties of the second order nonlinear susceptibility

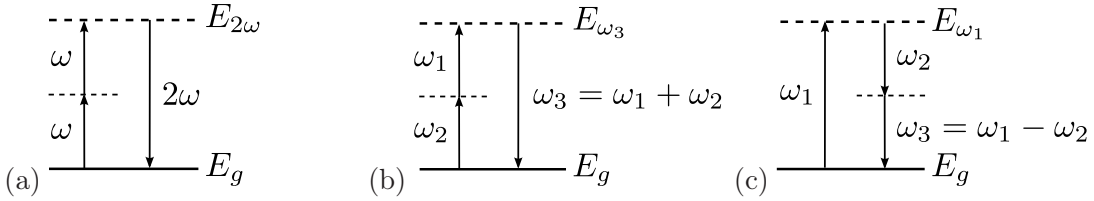

Figure 3.1: Energy-level diagrams of second-harmonic (a), sum-frequency (b) and difference-frequency (c) generation. Graph (c) also describes SPDC.

$\chi^{(2)}$. In the full vector approach, susceptibility $\chi^{(2)}_{ijk}$ (i,j,k=x,y,z) is the third rank tensor, which consists 27 Cartesian components. Therefore, all 324 complex numbers have to be determined for its full definition. However, symmetry properties allow to lower this number. First of all, since the electric-field and induced-polarization in Eq. (3.1) describe real physical quantities, all components of $\chi^{(2)}_{ijk}$ must obey $\chi^{(2)*}_{ijk}(\omega) = \chi^{(2)}_{ijk}(-\omega)$. Susceptibility $\chi^{(2)}$ has to also satisfy the intrinsic permutation symmetry. In the case of loss-less crystal, $\chi^{(2)}$ has all components real and $\chi^{(2)}$ hence shows the full permutation symmetry. If the frequencies of interacting waves are far from atom or molecular resonances, dispersion of nonlinear susceptibility can be omitted and the Kleinman symmetry is reached. Other reduction of the number of independent coefficients of susceptibility $\chi^{(2)}$ is reached, when spatial properties of a crystal are taken into account [40]. For centro-symmetric materials $\chi^{(2)}$ vanishes.

3.2 Quantization of Electromagnetic Field

In order to reach the full quantum approach of non-linear phenomena, we utilize quantization of the electromagnetic field [41, 42]. The first quantization procedure starts by introducing the vectorial potential $\mathbf{A}$ and the scalar potential ϕ. Then we can express the magnetic-field flux and the electric-field amplitude in the form:

$$\mathbf{B} = \mathrm{rot}\mathbf{A}, \tag{3.3}$$

$$\mathbf{E} = -\nabla\phi - \frac{\partial \mathbf{A}}{\partial t}. \tag{3.4}$$

The Coulomb gauge requires $\mathrm{div}\mathbf{A} = 0$ and $\phi = 0$. From the source-free Maxwell equations in a dielectric medium, the wave equation for the vectorial potential $\mathbf{A}$ is equal to:

$$\Delta\mathbf{A} - \frac{\left(1+\chi^{(1)}\right)}{c^2}\frac{\partial^2 \mathbf{A}}{\partial t^2} = 0. \tag{3.5}$$

The solution is assumed with the following time dependence $\mathbf{A}_{\alpha\mathbf{k}}(\mathbf{r},t) = \mathbf{A}_{\alpha\mathbf{k}}(\mathbf{r}).e^{i\omega_{\mathbf{k}}t}$. Periodic boundary conditions allow us to express $\mathbf{A}_{\alpha\mathbf{k}}(\mathbf{r}) = N_{\mathbf{k}}.\mathbf{e}_{\alpha\mathbf{k}}.e^{i\mathbf{k}.\mathbf{r}}$. The symbol $N_{\mathbf{k}}$ stands for the normalization constant and $\mathbf{e}_{\alpha\mathbf{k}}$ is the unit polarization vector of polarization $\alpha = \mathrm{TE}, \mathrm{TM}$. The magnitude of wave-vector $\mathbf{k}$ is equal to $k^2 = \omega_k^2/v_k^2 = k_x^2 + k_y^2 + k_z^2$.

The final solution can be expressed as the Fourier series:

$$\mathbf{A}\left(\mathbf{r},t\right) = \sum_{\mathbf{k}} \sum_{\alpha=TE,TM} N_{\mathbf{k}} \left(\mathbf{e}_{\alpha\mathbf{k}} a_{\alpha\mathbf{k}}\left(t\right) e^{i\mathbf{k}.\mathbf{r}} + \mathbf{e}^*_{\alpha\mathbf{k}} a^*_{\alpha\mathbf{k}}\left(t\right) e^{-i\mathbf{k}.\mathbf{r}} \right), \tag{3.6}$$

where the functions $a_{\alpha\mathbf{k}}(t)$ are Fourier coefficients. Substituting Eq. (3.6) to Eq. (3.4) the electric-field amplitude reaches the form:

$$\mathbf{E}\left(\mathbf{r},t\right) = \sum_{\mathbf{k}} \sum_{\alpha=TE,TM} N_{\mathbf{k}} i\omega_k \left(\mathbf{e}_{\alpha\mathbf{k}} a_{\alpha\mathbf{k}}\left(t\right) e^{i\mathbf{k}.\mathbf{r}} - \mathbf{e}^*_{\alpha\mathbf{k}} a^*_{\alpha\mathbf{k}}\left(t\right) e^{-i\mathbf{k}.\mathbf{r}} \right). \tag{3.7}$$

We have assumed the Fourier coefficients of the form $a_{\alpha\mathbf{k}}(t) = a_{\alpha\mathbf{k}}(0).e^{-i\omega_{\mathbf{k}}t}$. In a similar way, we can express the magnetic-field flux defined in Eq. (3.3) as:

$$\mathbf{B}\left(\mathbf{r},t\right) = \sum_{\mathbf{k}} \sum_{\alpha=TE,TM} N_{\mathbf{k}} i \left[\left(\mathbf{k} \times \mathbf{e}_{\alpha\mathbf{k}}\right) a_{\alpha\mathbf{k}}\left(t\right) e^{i\mathbf{k}.\mathbf{r}} - \left(\mathbf{k} \times \mathbf{e}^*_{\alpha\mathbf{k}}\right) a^*_{\alpha\mathbf{k}}\left(t\right) e^{-i\mathbf{k}.\mathbf{r}} \right]. \tag{3.8}$$

Hamiltonian of the electromagnetic field in a dielectric medium with negligible dispersion is equal to:

$$H = \int_V d\mathbf{r} \left(\varepsilon_0 \varepsilon_r \mathbf{E}^2 + \frac{1}{\mu 0} \mathbf{B}^2 \right) = \int_V d\mathbf{r} \left[\varepsilon_0 \varepsilon_r \left(-\frac{\partial \mathbf{A}}{\partial t} \right)^2 + \frac{1}{\mu 0} \left(\mathrm{rot}\mathbf{A} \right)^2 \right], \tag{3.9}$$

where the relative permittivity $\varepsilon_r = 1 + \chi^{(1)}$, ϵ_0 is the vacuum permittivity and V is the interaction volume. This Hamiltonian can be modified using Eq. (3.6) to:

$$H = V \varepsilon_0 \varepsilon_r \sum_{\mathbf{k}} \sum_{\alpha=TE,TM} N_{\mathbf{k}}^2 \omega_{\mathbf{k}}^2 \left[a_{\alpha\mathbf{k}}\left(t\right) a^*_{\alpha\mathbf{k}}\left(t\right) + a^*_{\alpha\mathbf{k}}\left(t\right) a_{\alpha\mathbf{k}}\left(t\right) \right]. \tag{3.10}$$

The explicit form of normalization function $N_{\mathbf{k}}$ is obtained by comparing this Hamiltonian in Eq. (3.10) with the Hamiltonian for the sum of energies of independent harmonic oscillators:

$$H = \sum_{\mathbf{k}} \sum_{\alpha=TE,TM} \hbar\omega_{\mathbf{k}} \left[a_{\alpha\mathbf{k}}\left(t\right) a^*_{\alpha\mathbf{k}}\left(t\right) + a^*_{\alpha\mathbf{k}}\left(t\right) a_{\alpha\mathbf{k}}\left(t\right) \right], \tag{3.11}$$

where $\hbar$ is the reduced Planck constant. We find that

$$N_{\mathbf{k}} = \sqrt{\frac{\hbar}{2V\varepsilon_0\varepsilon_r\omega_{\mathbf{k}}}}. \tag{3.12}$$

Until now we have considered that the Fourier coefficients are complex functions. The quantization of field is accomplished when we perform the exchange of complex functions $a_{\alpha\mathbf{k}}(t)$ and $a^*_{\alpha\mathbf{k}}(t)$ by bosonic operators $\hat{a}_{\alpha\mathbf{k}}(t)$ and $\hat{a}^\dagger_{\alpha\mathbf{k}}(t)$. The symbol $\dagger$ stands for the Hermitian conjugation. These operators are required to satisfy the bosonic equal-time commutation relations $[\hat{a}_{\alpha\mathbf{k}}(t), \hat{a}^\dagger_{\alpha'\mathbf{k}'}(t)] = \delta_{\alpha\alpha'}\delta_{\mathbf{k}\mathbf{k}'}$. In the last step, we express the electric-field $\mathbf{E}$ in the final form:

$$\hat{\mathbf{E}}(\mathbf{r},t) = \sum_{\mathbf{k}}\sum_{\alpha} i\sqrt{\frac{\hbar\omega_{\mathbf{k}}}{2V\varepsilon_0\varepsilon_r}}\left(\mathbf{e}_{\alpha\mathbf{k}}\hat{a}_{\alpha\mathbf{k}}(t)\,e^{i\mathbf{k}.\mathbf{r}} - \mathbf{e}^*_{\alpha\mathbf{k}}\hat{a}^\dagger_{\alpha\mathbf{k}}(t)\,e^{-i\mathbf{k}.\mathbf{r}}\right). \tag{3.13}$$

3.3 Description of Spontaneous Parametric Downconversion

Spontaneous parametrical downconversion in nonlinear materials is one of the most fascinating nonlinear optical effects. It has been theoretically predicted by Louisell et al. in 1961 [43, 44]. In the SPDC process, a strong pump-field non-resonantly interacts with atoms or molecules of a nonlinear medium and gives rise to an emission of two photons, called from the historical reason a signal and an idler photon. The emission of down-converted photon pairs is caused by random vacuum fluctuations and so the emission time is unknown. Since photons in a pair are created together in a particular spatial point, they are strongly correlated in time [45]. Their mutual properties are influenced by the following conditions:

$$\hbar\omega_p = \hbar\omega_s + \hbar\omega_i, \tag{3.14}$$

$$\mathbf{k}_p = \mathbf{k}_s + \mathbf{k}_i. \tag{3.15}$$

Eq. (3.14) corresponds to the energy-conservation law and Eq. (3.15) is the momentum conservation law. Both equations determine phase-matching conditions. They are discussed in detail in the next chapter 4.

The SPDC process is conventionally described by the following multi-mode interac-

tion Hamiltonian $\hat{H}_{\rm int}$ [46, 47] written in the interaction picture:

$$\begin{aligned}\hat{H}_{\rm int}(t) &= \varepsilon_0 \int_{\mathcal{B}} d\mathbf{r}_\perp \int_{-L}^{0} dz \chi^{(2)}(z) : \mathbf{E}_p^{(+)}(\mathbf{r}_\perp, z, t)\hat{\mathbf{E}}_s^{(-)}(\mathbf{r}_\perp, z, t)\hat{\mathbf{E}}_i^{(-)}(\mathbf{r}_\perp, z, t) \\ &+ \text{H.c.}, \end{aligned} \tag{3.16}$$

where L denotes the crystal length and $\mathcal{B}$ means the transverse area of optical fields. The z-dependent second-order susceptibility tensor $\chi^{(2)}$ describes non-linearity in a material. We would like to stress that the Hamiltonian in Eq. (3.16) is also responsible for the generation of multi-mode squeezed light [48, 49]. In Eq. (3.16), the positive-frequency part of classical pump electric-field amplitude is denoted as $\mathbf{E}_p^{(+)}$. $\hat{\mathbf{E}}_s^{(-)}$ ($\hat{\mathbf{E}}_i^{(-)}$) stands for the negative-frequency part of the signal (idler) electric-field amplitude operator defined in Eq. (3.13).

Equation (3.13) can be simplified as follows. We replace $\sum_{\mathbf{k}}$ by $V/(2\pi)^3 \int d\mathbf{k}$ and consider only the collinear propagation. Thus we omit the dependence of electric-fields on the transversal coordinates $\mathbf{r}_\perp$. We also assume only one polarization for the signal and idler fields. Then the electric-field amplitudes $\hat{\mathbf{E}}_a^{(-)}$ $a = s, i$ take the form:

$$\begin{aligned}\hat{\mathbf{E}}_a^{(-)}(z,t) &= \frac{1}{2\pi}\int d\omega_a \hat{\mathbf{E}}_a^{(-)}(\omega_a)\exp(-ik_a z + i\omega_a t), \\ &\qquad a = s, i, \end{aligned} \tag{3.17}$$

where the quantum spectral amplitudes $\hat{\mathbf{E}}_a^{(-)}(\omega_a)$ can be expressed using the photon creation operators $\hat{a}_a^\dagger(\omega_a)$:

$$\hat{\mathbf{E}}_a^{(-)}(\omega_a) = -i\sqrt{\frac{\hbar\omega_a}{2\varepsilon_0 c n_a \mathcal{B}}}\hat{a}_a^\dagger(\omega_a)\mathbf{e}_{a\omega}^*, \tag{3.18}$$

the symbol n_a is the index of refraction and $\varepsilon_{r,a} = n_a^2$.

First-order perturbation solution of the Schrödinger equation:

$$i\hbar\frac{\partial|\psi\rangle}{\partial t} = \hat{H}_{int}(t)|\psi\rangle \tag{3.19}$$

with the initial vacuum state $|\text{vac}\rangle$ in the signal and idler fields and the Hamiltonian of Eq. (3.19) give the following two-photon quantum state $|\psi\rangle$:

$$|\psi\rangle = \int d\omega_s \int d\omega_i \Phi(\omega_s, \omega_i)\hat{a}_s^\dagger(\omega_s)\hat{a}_i^\dagger(\omega_i)|\text{vac}\rangle. \tag{3.20}$$

The two-photon spectral amplitude Φ introduced in Eq. (3.20) is given as follows:

$$\Phi(\omega_s, \omega_i) = g(\omega_s, \omega_i) E_p^{(+)}(\omega_s + \omega_i) F(\Delta k(\omega_s, \omega_i)), \tag{3.21}$$

where g denotes the coupling constant, $g(\omega_s, \omega_i) = i\sqrt{\omega_s \omega_i}/[2c\pi\sqrt{n_s(\omega_s) n_i(\omega_i)}]\chi^{(2)}(0)$, and $E_p^{(+)}(\omega_p)$ stands for the pump-field amplitude spectrum. Symbol $\chi^{(2)}(0)$ means an effective value of nonlinear susceptibility after tensor contraction. The stochastic function F introduced in Eq. (3.21) describes phase-matching and attains the form:

$$F(\Delta k) = \int_{-L}^{0} dz \, \frac{\chi^{(2)}(z)}{\chi^{(2)}(0)} \exp(i\Delta k z). \tag{3.22}$$

Symbol Δk describes the natural phase mismatch for the interacting fields, $\Delta k = k_p - k_s - k_i$.

Since we are interested in periodically poled crystals (see chapter 4), where neighbor domains differ in signs of $\chi^{(2)}$ nonlinearity, we can the function F defined in Eq. (3.22) recast into the form:

$$F(\Delta k) = \sum_{n=1}^{N_L} (-1)^{n-1} \int_{z_{n-1}}^{z_n} dz \exp(i\Delta k z). \tag{3.23}$$

Symbol N_L denotes the number of domains (layers) and n-th domain extends from $z = z_{n-1}$ to $z = z_n$.

In randomly poled crystals studied in chapters 5 and 6 the positions z_n of domain boundaries are random and can be expressed as $z_n = z_{n-1} + l_0 + \delta l_n$ ($n = 1, \ldots, N_L$, $z_0 = -L$) in our model using stochastic Gaussian declinations δl_n. The basic layer length l_0 is determined such that quasi-phase-matching is reached (for details see chapter 4), i.e. $l_0 = \pi/\Delta k_0$, $\Delta k_0 \equiv \Delta k(\omega_s^0, \omega_i^0)$, and ω_a^0 means the central frequency of field a. The random declinations δl_n are mutually independent and can be described by the joint Gaussian probability distribution P:

$$P(\delta \mathbf{L}) = \frac{1}{(\sqrt{\pi}\sigma)^{N_L}} \exp(-\delta \mathbf{L}^T \mathbf{B} \delta \mathbf{L}). \tag{3.24}$$

Covariance matrix $\mathbf{B}$ is assumed to be diagonal and its nonzero elements equal $1/\sigma^2$. Stochastic vector $\delta \mathbf{L}$ is composed of declinations δl_n; symbol ^{T} stands for transposition.

Characteristic function G of the distribution P in Eq. (3.24) takes the form:

$$G(\delta\mathbf{K}) \equiv \langle \exp(i\delta\mathbf{K}\cdot\delta\mathbf{L})\rangle_{\mathrm{av}} = \prod_{j=1}^{N} G(\delta k_j). \tag{3.25}$$

Vector $\delta\mathbf{K}$ of parameters of the characteristic function G is composed of elements δk_j. One-dimensional characteristic function $G(\delta k)$ in Eq. (3.25) equals $\exp(-\sigma^2\delta k^2/4)$.

In order to obtain analytical formulas (namely in section 5.2), we integrate the expression for function F in Eq. (3.23) domain by domain and modify the contributions of the first and last domains in such a way that the following simple formula is reached:

$$F(\Delta k) = \frac{2i}{\Delta k}\sum_{n=0}^{N_L}(-1)^n \exp(i\Delta k z_n). \tag{3.26}$$

As a typical structure contains hundreds of domains, incorrect inclusion of fields from the first and the last domains leads to negligible declinations.

Photon-pair generation rate as well as intensity spectra can be easily derived from mean spectral density of the number of generated photon pairs $n(\omega_s,\omega_i)$. The mean spectral density n corresponding to the quantum state $|\psi\rangle$ is defined by the formula:

$$n(\omega_s,\omega_i) = \langle\langle\psi|\hat{a}_s^\dagger(\omega_s)\hat{a}_s(\omega_s)\hat{a}_i^\dagger(\omega_i)\hat{a}_i(\omega_i)|\psi\rangle\rangle_{\mathrm{av}}, \tag{3.27}$$

where the symbol $\langle\rangle_{\mathrm{av}}$ means stochastic averaging over an ensemble of geometric configurations of a crystal. Assuming the quantum state $|\psi\rangle$ written in Eq. (3.20) we arrive at the formula:

$$n(\omega_s,\omega_i) \;=\; |g(\omega_s,\omega_i)|^2 |E_p^{(+)}(\omega_s+\omega_i)|^2 \langle |F(\Delta k(\omega_s,\omega_i))|^2\rangle_{\mathrm{av}}. \tag{3.28}$$

Spectrum S_s of, e.g., the signal field and photon-pair generation rate N can then be derived using the expressions:

$$S_s \;=\; \hbar\omega_s \int d\omega_i n(\omega_s,\omega_i), \tag{3.29}$$

$$N \;=\; \int d\omega_s \int d\omega_i n(\omega_s,\omega_i) \tag{3.30}$$

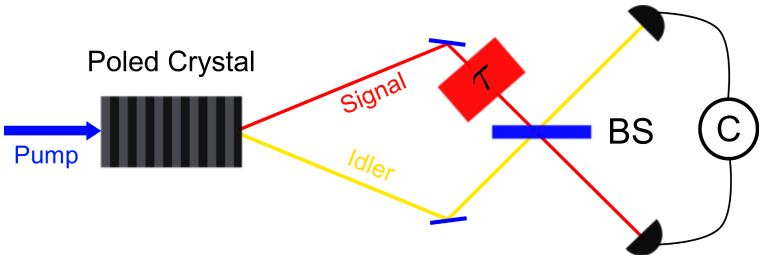

Figure 3.2: Scheme of a Hong-Ou-Mandel interferometer, where BS stands for the beam splitter and C stands for the coincidence-count measurement device.

3.4 Hong-Ou-Mandel Interference and Correlation Time

As it has been mentioned above, signal and idler photons are strongly correlated because both photons are generated inside the nonlinear medium at one instant. A finite distance between the detection times of both photons is a consequence of dispersion properties of the nonlinear medium through which both photons at different frequencies propagate before they leave the crystal. Temporal correlations of the signal and idler photons can be conveniently described using a two-photon temporal amplitude $\mathcal{A}$ defined as:

$$\mathcal{A}(t_s, t_i) = \langle \mathrm{vac} | \hat{E}_s^{(+)}(t_s) \hat{E}_i^{(+)}(t_i) | \psi \rangle. \tag{3.31}$$

This amplitude $\mathcal{A}(t_s, t_i)$ gives the probability amplitude of detecting a signal photon at time t_s and an idler photon at time t_i.

The simplest experimental method for the determination of a typical constant characterizing temporal width of the two-photon detection window (entanglement time) uses a Hong-Ou-Mandel interferometer [50]. In this interferometer, the signal and idler fields mutually interfere on a beam-splitter and photons leaving the beam-splitter at different output ports are subsequently detected in a coincidence-count measurement. The coincidence-count rate R_n depends on a mutual time delay τ introduced between the signal and idler photons. The time delay can be introduced to the signal path as presented in Fig. 3.2. It can be shown that temporal extension of the interference part in the coincidence-count rate R_n is proportional to entanglement time under certain conditions. The coincidence-count rate R_n as a function of relative time delay τ is described by the following formula:

$$R_n(\tau) = 1 - \varrho(\tau), \tag{3.32}$$

where:

$$\rho(\tau) = \frac{1}{2R_0}\int_{-\infty}^{\infty} dt_1 \int_{-\infty}^{\infty} dt_2 \mathrm{Re}\left[\langle \mathcal{A}(t_1, t_2-\tau)\mathcal{A}^*(t_2, t_1-\tau)\rangle_{\mathrm{av}}\right], \tag{3.33}$$

$$R_0 = \frac{1}{2}\int_{-\infty}^{\infty} dt_1 \int_{-\infty}^{\infty} dt_2 \langle |\mathcal{A}(t_1, t_2)|^2\rangle_{\mathrm{av}}. \tag{3.34}$$

Inserting Eqs. (3.20) and (3.21) for the quantum state $|\psi\rangle$ and two-photon temporal amplitude $\mathcal{A}$ into Eqs. (3.33) and (3.34) we arrive at the expressions:

$$\rho(\tau) = \frac{\pi\hbar^2}{4\epsilon_0^2 c^2 \mathcal{B}^2}\frac{1}{R_0}\mathrm{Re}\left[\int_0^{\infty} d\omega_s \int_0^{\infty} d\omega_i\ \omega_s\omega_i \langle \Phi(\omega_s, \omega_i)\Phi^*(\omega_i, \omega_s)\rangle_{\mathrm{av}} \times \exp(i\omega_i\tau)\exp(-i\omega_s\tau)\right], \tag{3.35}$$

$$R_0 = \frac{\pi\hbar^2}{4\epsilon_0^2 c^2 \mathcal{B}^2}\int_0^{\infty} d\omega_s \int_0^{\infty} d\omega_i\ \omega_s\omega_i \langle |\Phi(\omega_s, \omega_i)|^2\rangle_{\mathrm{av}}. \tag{3.36}$$

Characteristics of temporal correlations (correlation time) between the signal and idler fields can also be obtained from the measurement of sum-frequency intensity in a nonlinear medium combining the signal and idler photons and having a sufficiently high value of $\chi^{(2)\mathrm{sum}}$ nonlinearity. This process allows us to determine the temporal correlation function I^{sum} of intensities of the signal and idler fields [51]. Intensity I^{sum} of the sum-frequency field is given along the formula:

$$I^{\mathrm{sum}}(\tau) = \eta^{\mathrm{sum}}\int_{-\infty}^{\infty} dt \left|\langle \mathrm{vac}|\hat{E}_s^{(+)}(t)\hat{E}_i^{(+)}(t-\tau)|\psi\rangle\right|^2, \tag{3.37}$$

where constant η^{sum} incorporates the value of $\chi^{(2)\mathrm{sum}}$ nonlinearity and quantum detection efficiency.

Chapter 4

Phase-Matching Techniques of the Interacting Fields

4.1 Phase-Matching

As it has been previously mentioned in chapter 3, the non-linear optical process of SPDC depends strongly on phase matching (PM) of the interacting fields, which is characterized via the phase-mismatch function Δk. Perfect phase-matching occurs only when $\Delta k = 0$ and the energy of pump field is effectively transferred to two daughter photons only under this circumstance. Perfect phase matching can be also understood on the molecular level, since each dipole moment radiates independently, however, when the phase-matching condition is met, they radiate together in the phase and the same direction.

Since the most of nonlinear materials used in optics exhibit normal dispersion, phase matching is usually hard to reach. The easiest ways how to naturally ensure PM are the utilization of differences between indices of refraction for the ordinary and extraordinary waves in birefringent crystals [52] and the use of different angles of propagation of the fields. In the latter case, spatial walk-off may reduce the conversion efficiency. According to the polarization of fields, the interaction is Type-0 when all fields have the same polarization, Type-I when the pump field has an orthogonal polarization with respect to the emitted fields having the same polarization, or Type-II when the emitted fields have mutually orthogonal polarizations. In waveguides, PM can be reached between different guided spatial modes. Semiconductor Bragg reflection waveguides are typical examples, where PM is reached for a pump field propagating as the Bragg mode and down-converted fields as totally internally reflected modes [17, 53, 54]. The scheme of

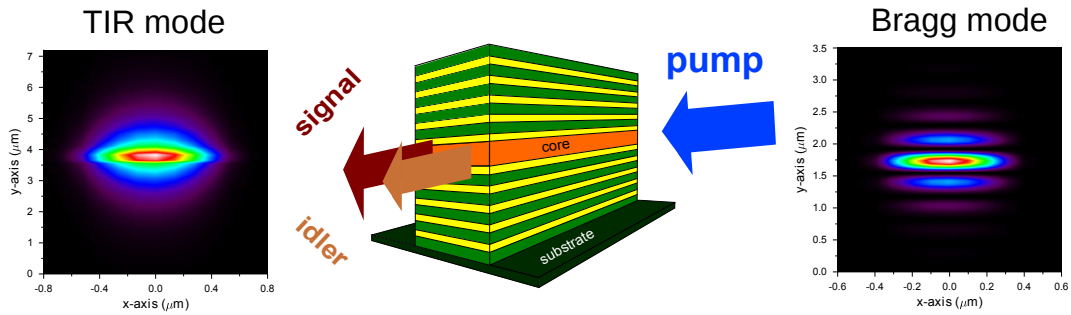

Figure 4.1: Example of modal phase matching of different guided modes in a Bragg reflection waveguide with SPDC process [A5,A6,A15].

SPDC in Bragg reflection waveguides is presented in Fig. 4.1. Alternatively, PM can be also achieved via an artificial birefringence in a layered slab (waveguides) as has been shown in [55].

Dispersion properties of the fields in both bulk and waveguide geometries determine spatio-temporal characteristics of generated fields. It is convenient to express the phase-mismatch function Δk using the Taylor series expansion in all fields:

$$\begin{aligned}\Delta k = k_p - k_s - k_i \quad &= \quad (k_{p0} - k_{s0} - k_{i0}) + \\ &+ \quad \left.\frac{\partial k_p}{\partial \omega_p}\right|_{\omega_{p0}} d\omega_p - \left.\frac{\partial k_s}{\partial \omega_s}\right|_{\omega_{s0}} d\omega_s - \left.\frac{\partial k_i}{\partial \omega_i}\right|_{\omega_{i0}} d\omega_i + \\ &+ \quad \left.\frac{\partial^2 k_p}{\partial \omega_p^2}\right|_{\omega_{p0}} d\omega_p^2 - \left.\frac{\partial^2 k_s}{\partial \omega_s^2}\right|_{\omega_{s0}} d\omega_s^2 - \left.\frac{\partial^2 k_i}{\partial \omega_i^2}\right|_{\omega_{i0}} d\omega_i^2 + \ldots \quad (4.1)\end{aligned}$$

The first term on the right-hand side of Eq. (4.1) represents the phase difference for the central frequencies of all fields. The terms located on the second line correspond to the phase acquired via the difference of inverted values of group velocities $\left.\frac{\partial k_a}{\partial \omega_a}\right|_{\omega_{a0}}$ for $a = p, s, i$. These terms are dominant for Type-II interaction. Terms on the third line correspond to the phase obtained due to the different dispersion of group velocities of fields $\left.\frac{\partial^2 k_a}{\partial \omega_a^2}\right|_{\omega_{a0}}$ for $a = p, s, i$. On the other hand, these terms are dominant for Type-0 and Type-I interactions.

4.2 Quasi-Phase-Matching

Unfortunately, a large amount of materials suitable for light-conversion applications is incapable to achieve PM of SPDC in a natural way. In 1962 Armstrong has come with an idea of periodical modulation of nonlinear susceptibility in other to compensate

natural phase mismatch [56]. This approach is known as quasi-phase-matching (QPM) at present. This periodic modulation of $\chi^{(2)}$ induces an additional wave-vector k_{QPM} to PM conditions, which allows to preclude the back-conversion. This wave vector originates from the condition $k_{QPM} = \Delta k$. The purpose of periodic modulation is to ensure that the direction of flow of energy from the pump field is recovered after the coherence length $L_c = \pi/\Delta k$. The phase-matching equation for QPM has the form:

$$k_{p0} - k_{s0} - k_{i0} - \frac{2\pi m}{\lambda_{QPM}} = 0, \tag{4.2}$$

where $\lambda_{QPM} = 2\pi/k_{QPM}$ is a spatial period of the modulation and m is the order of QPM [57]. The Fourier transformation of the rectangular profile of modulation of $\chi^{(2)}(z)$, which is typical for periodically poled structures, allows to express an influence of modulation by means of reduced value of nonlinear susceptibility:

$$\chi^{(2)}_{QPM} = \chi^{(2)} \frac{2}{\pi m} \sin(m\pi D). \tag{4.3}$$

Symbol D stands for a duty cycle. As it is possible to observe, nonlinear process using QPM will be always less effective than the naturally phase-matched one. On the other hand, the QPM technique allows to utilize the highest components of nonlinear susceptibility $\chi^{(2)}$, which cannot be reached via natural PM. QPM can be achieved by different techniques as a stack of layers with alternating orientation of the crystal axis, periodic poling (see section 4.4) or using alternated domain grow in semiconductor materials [58–60].

4.3 Stochastic Quasi-Phase-Matching

In addition to the previously discussed phase-matching techniques, a random profile of susceptibility $\chi^{(2)}$ results in continuous erasing of the mutual-phase-information between the fields. Thus the unwanted back-conversion effect is negligible [61]. This technique is called stochastic quasi-phase-matching (SQPM). Despite the fact, that the efficiency of random structures has been found to be worse compared to the ordered ones, they usually put smaller requirements to polarization properties of the interacting optical fields as well as to the orientation of the nonlinear medium [A4]. Whereas QPM necessaryly involves additional fabrication techniques, SQPM can naturally occurs in materials like $Sr_{0.6}Ba_{0.4}Nb_2O_6$ (SBN) [62, 63]. Moreover, artificial randomly poled structures are easier to fabricate because of lower precision requirements.

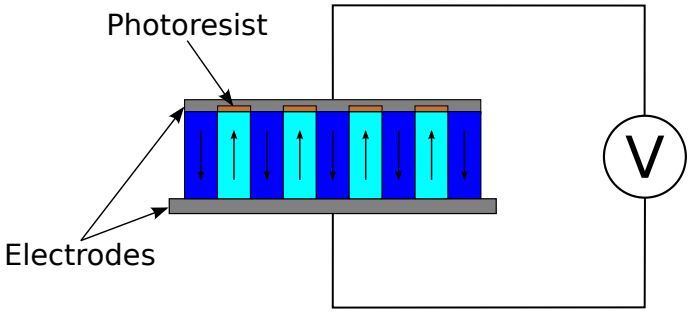

Figure 4.2: Sketch of the poling technique. A non-linear material is placed between electrodes. Arrows denote the orientation of ferroelectric domains.

The effect of SQPM in one dimension has already been addressed for the process of second-harmonic generation [64–68] and the process of difference-frequency generation [69]. Moreover full domain random structures allowing SQPM for transversal second-harmonic generation have been studied in [70]. An ultra-narrow spectral emission in SPDC in random layered media has been presented in [71].

4.4 Poling Technique

Periodic poling (PP) technique is the most common fabrication method for achieving QPM or SQPM in ferroelectric materials as $LiNbO_3$ [72], $LiTaO_3$ [73], KTA, and KTP [74]. The principle of poling process is presented in Fig. 4.2. The poling process starts with applying a photo-resist via the lithographic method according to the required poling pattern (reflecting the poling period) on the material in areas, which are not going to be inverted. Then electrodes are added on the material and a strong static electric field of intensity about tens of kilovolts is applied. This result in a permanent rotation of the orientation of ferroelectric domains in the areas of the present electric field. Therefore, the adjacent domains differ in their signs of non-linear susceptibility $\chi^{(2)}$, as it is required in the QPM technique.

Application of this method is limited to substrates with a thickness about few millimeters because of non-homogeneity of the applied electric field inside a sample. The PP method can be used to prepare different shapes of poling patterns of various poling periods, linearly chirped patterns [75, 76] and even randomly ordered patterns.

Chapter 5

Randomly Poled Nonlinear Crystals

5.1 Introduction

In this chapter, we present a numerical study of the generation of photon pairs in randomly poled 1D nonlinear crystals shown schematically in Fig. 5.1. The basic model of RPS has been described in section 3.3. As an example, we consider a spectrally degenerate (nearly) collinear SPDC from periodically-poled $LiNbO_3$ pumped at the wavelength $\lambda_p^0 = 775$ nm by a cw laser beam. The signal and idler photons thus occur at the fiber-optics communication wavelength $\lambda_s = \lambda_i = 1.55$ μm. The crystal optical axis is perpendicular to the fields' propagation direction and is parallel to the vertical direction. All fields are vertically polarized and so the largest element $\chi^{(2)}_{zzz} = 54pm/V$ of the susceptibility tensor is used. The natural phase mismatch for this configuration is compensated by the basic domain length l_0 equal to 9.51535 μm. A structure composed of $N_L = 700$ layers is roughly 6.5 mm long.

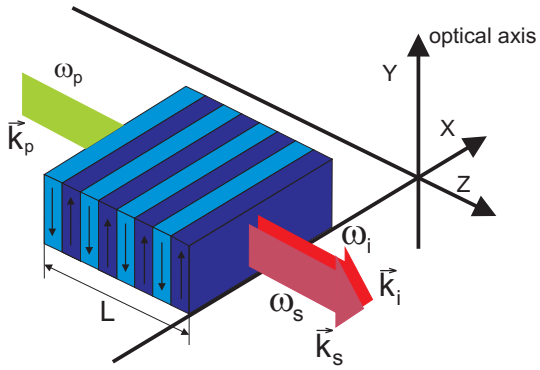

Figure 5.1: Geometry of SPDC in one dimensional RPS.

5.2 Analytical Expressions for Randomly Poled Crystals

Analytical expressions in this section are obtained using the results of section 3.3. The averaged squared modulus of the phase-matching function F as determined by the formula in Eq. (3.26) can be written in the form:

$$\langle|F(\Delta k)|^2\rangle_{\mathrm{av}} = \frac{4}{\Delta k^2}\left((N_L+1)\frac{1-|H(\delta k)|^2}{|1-H(\delta k)|^2} - \left[\frac{H(\delta k)[1-H(\delta k)^{N_L+1}]}{[1-H(\delta k)]^2} + \mathrm{c.c.}\right]\right), \tag{5.1}$$

$\delta k(\omega_s,\omega_i) = \Delta k(\omega_s,\omega_i) - \Delta k_0$. Symbol c.c. replaces the complex-conjugated term. Function $H(\delta k)$ occurring in Eq. (5.1) is defined as:

$$H(\delta k) = \exp[i\delta k l_0]G(\Delta k_0+\delta k), \tag{5.2}$$

$$G(\Delta k) = \exp\left(-\frac{\sigma^2\Delta k^2}{4}\right). \tag{5.3}$$

The averaged squared modulus $\langle|F(\Delta k)|^2\rangle_{\mathrm{av}}$ of phase-matching function given in Eq. (5.1) determines the averaged spectral density n and behaves as follows. It holds that $|H| \leq 1$ and $|H| = 1$ for a fully ordered structure. If $\delta k = 0$ in a fully ordered structure, H is real ($H = 1$) and the averaged squared phase-matching function $\langle|F(\Delta k)|^2\rangle_{\mathrm{av}}$ reaches its maximum value $4(N_L+1)^2$. Nonzero phase mismatch δk shifts H into the complex plane which results in lower values of the mean value $\langle|F(\Delta k)|^2\rangle_{\mathrm{av}}$. The larger the δk, the smaller the mean value $\langle|F(\Delta k)|^2\rangle_{\mathrm{av}}$. Inspection of the formula for H in Eq. (5.3) also shows that the larger the value of the basic layer length l_0 the faster the decrease of mean values $\langle|F(\Delta k)|^2\rangle_{\mathrm{av}}$ for given δk. According to the formula in Eq. (5.3) the larger the standard deviation σ of a random structure the smaller the value of $|H|$. The decrease of values of $|H|$ results in an increase of the range of values of the phase mismatch δk in which the averaged squared modulus $\langle|F(\Delta k)|^2\rangle_{\mathrm{av}}$ of phase-matching function attains non-negligible values [see the formula in Eq. (5.1)].

The formula for averaged squared modulus $\langle|F(\Delta k)|^2\rangle_{\mathrm{av}}$ of phase-matching function in Eq. (5.1) can be substantially simplified under the assumption $\sigma^2(\Delta k_0)^2 N_L/2 \gg 1$:

$$\langle|F(\Delta k)|^2\rangle_{\mathrm{av}} = \frac{2N_L\left[1-G(\Delta k_0+\delta k)\right]}{(\Delta k_0+\delta k)^2\left[1-2G(\Delta k_0+\delta k)\cos(\delta k l_0)+G(\Delta k_0+\delta k)^2\right]}. \tag{5.4}$$

Increasing values of phase mismatch δk lead to greater values of the denominator in the fraction on the right-hand-side of Eq. (5.4) that result in the decrease of values of the averaged squared modulus $\langle|F(\Delta k)|^2\rangle_{\mathrm{av}}$ of phase-matching function. On the other

hand, increasing values of deviation σ weaken this behavior.

For comparison, we consider another type of RPS defined such that $z_n = -L + nl_0 + \delta l_n$ where δl_n is a random declination of the n-th boundary. These 'weakly-random' structures are more ordered compared to those considered earlier because the change of length of an n-th domain is compensated by the change in length of an $(n+1)$-th domain. The averaged squared modulus $\langle |F^{\mathrm{w-r}}(\Delta k)|^2 \rangle_{\mathrm{av}}$ of phase-matching function can be derived in this case as follows:

$$\begin{aligned}\langle |F^{\mathrm{w-r}}(\Delta k)|^2 \rangle_{\mathrm{av}} &= \frac{4}{(\Delta k)^2} \Bigg\{ N_L + 1 + |G(\Delta k_0 + \delta k)|^2 \left[\frac{\exp(i\delta k l_0)}{1 - \exp(i\delta k l_0)} \right. \\ &\times \left. \left(N_L - \exp(i\delta k l_0) \frac{1 - \exp[i\delta k l_0 N_L]}{1 - \exp(i\delta k l_0)} \right) + \mathrm{c.c.} \right] \Bigg\}. \end{aligned} \tag{5.5}$$

Disorder of the boundary positions manifests itself as a filter for the averaged squared modulus $\langle |F^{\mathrm{w-r}}(\Delta k)|^2 \rangle_{\mathrm{av}}$ of phase-matching function, as evident from the expression in Eq. (5.5). This leads to spectral filtering of the spectral density n. This behavior is qualitatively different from that observed in RPS as described by the formula in Eq. (5.1) indicating broadening of the spectral density n with increasing values of the deviation σ.

Spectral broadening is the most interesting feature of ordered chirped periodically poled structures (CPPS) that we consider here for comparison. Positions of boundaries in these structures are described by the formula $z_n = -L + nl_0 + \zeta'(n - N_L/2)^2 l_0^2$, $\zeta' = \zeta/\Delta k_0$, and ζ denotes chirping parameter. The phase-matching function $F^{\mathrm{chirp}}(\Delta k)$ then takes the form [77]:

$$\begin{aligned} F^{\mathrm{chirp}}(\Delta k) &= \frac{2\sqrt{\pi}}{\sqrt{i\Delta k^3 \zeta'}\, l_0} \exp(i\Delta k N_L l_0/2) \\ &\times \exp\left(-\frac{i\delta k^2}{4\Delta k \zeta'} \right) \left[\mathrm{erf}(f(N_L/2)) - \mathrm{erf}(f(-N_L/2)) \right], \end{aligned} \tag{5.6}$$

$$f(x) = \frac{\sqrt{-i}}{2} \left[\sqrt{\zeta'(\Delta k_0 + \delta k)}\, x l_0 + \frac{\delta k}{\sqrt{\zeta'(\Delta k_0 + \delta k)}} \right]. \tag{5.7}$$

The error function erf is defined as $\mathrm{erf}(x) = 2/\sqrt{\pi} \int_0^x \exp(-y^2) dy$. Detailed inspection of the formula in Eq. (5.6) reveals that the larger the value of chirping parameter ζ' the broader the phase-matching function $F^{\mathrm{chirp}}(\Delta k)$.

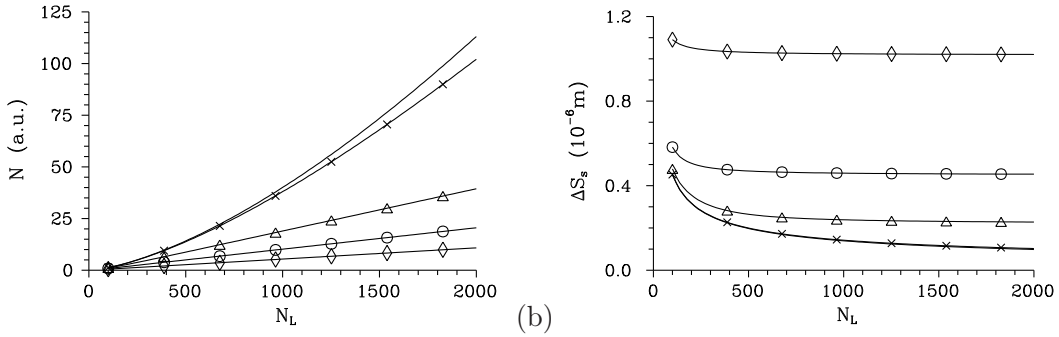

Figure 5.2: (a) Photon-pair generation rate N and (b) signal-field spectral width ΔS_s (FWHM) as functions of the number N_L of domains for an ensemble of RPSs with standard deviation σ equal to 0 m (solid curve), 0.1 $\times 10^{-6}$m (solid curve with $\times$), 0.5 $\times 10^{-6}$m (solid curve with $\triangle$), 1 $\times 10^{-6}$m (solid curve with $\circ$), and 2 $\times 10^{-6}$m (solid curve with $\diamond$); a.u. stands for arbitrary units.

5.3 Generation Rate and Spectral Properties

The most striking feature of RPSs is that the photon-pair generation rate N increases linearly with the number N_L of domains, independently of the standard deviation σ of the random positions of boundaries [see Fig. 5.2(a)]. Standard deviation σ plays the central role in the determination of spectral widths ΔS_s and ΔS_i of the signal and idler fields. The larger the value of deviation σ the broader the signal- and idler-field spectra S_s and S_i, as documented in Fig. 5.2(b). This behavior is easily understandable because structures generated with larger values of σ have statistically a broader spatial spectrum of the $\chi^{(2)}(z)$ modulation which gives more freedom for the fulfillment of quasi-phase-matching conditions. It holds that the broader the signal- and idler-field spectra S_s and S_i the smaller the photon-pair generation rate N [compare Figs. 5.2(a) and (b)]. It reflects the fact that constructive interference of fields from different domains is enhanced in the area outside the central frequencies ω_s^0 and ω_i^0 whereas this interference is weaken in the area around the central frequencies.

The photon-pair generation rate N increases roughly linearly with the number N_L of domains also in the case of 'weakly-random' structures described by the averaged squared modulus $\langle |F^{\mathrm{w-r}}(\Delta k)|^2 \rangle_{\mathrm{av}}$ of phase-matching function in Eq. (5.5), as shown in Fig. 5.3. The greater the standard deviation σ the smaller the photon-pair generation rate N. As for the signal-field spectral width ΔS_s its values do not practically depend on the variance σ.

The behavior of photon-pair generation as observed in RPSs can also be found in ordered CPPSs. Also here photon-pair generation rate N is linearly proportional to

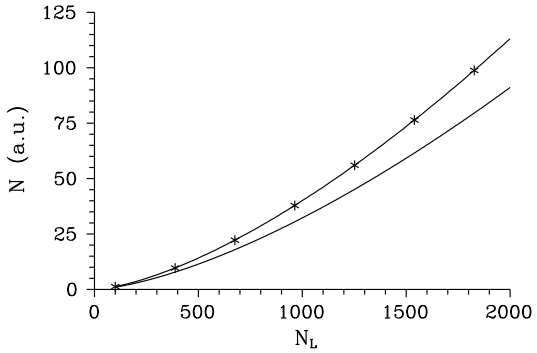

Figure 5.3: Photon-pair generation rate N as it depends on the number N_L of domains for an ensemble of 'weakly-random' structures with standard deviation σ equal to 0 m (solid curve with $*$) and 2 $\times 10^{-6}$m (solid curve).

the number N_L of domains and spectral widths ΔS_s and ΔS_i increase with increasing chirping parameter ζ. The main result of our analysis is that this similarity is both qualitative and quantitative. For any value of the chirping parameter ζ there exists a value of the standard deviation σ such that spectral widths ΔS_s and ΔS_i of the generated signal and idler fields are the same. Moreover, also photon-pair generation rates N are comparable. This is illustrated in Fig. 5.4 for a chirped structure with $N_L = 700$ domains. Its signal-field spectrum S_s is extraordinarily broad (larger that 1 μm) for sufficiently large values of the chirping parameter ζ [see Fig. 5.4(a)]. Signal-field spectra S_s of the same width can also be generated from RPSs with sufficiently large randomness (i.e., having large values of the deviation σ). Values of the standard deviation σ corresponding to the values of chirping parameter ζ are plotted in Fig. 5.4(b). Photon-pair generation rates N for RPSs and CPPSs are drawn for comparison in Fig. 5.4(c) in this case. Whereas CPPSs give better photon-pair generation rates N for larger values of chirping parameter ζ, RPSs even slightly overcome on average CPPSs for smaller values of ζ. Moreover, the signal-field spectra S_s of individual realizations may even be broader which results in sharper temporal features. On the other hand, these spectra are typically composed of many local peaks (see Fig. 5.5). RPSs thus represent an alternative broadband and efficient source of photon pairs with properties comparable to CPPSs. We note, that histograms of domain lengths corresponding to RPSs are broader compared to those characterizing CPPSs.

Alternatively, RPSs and CPPSs can be compared under the requirement of equal photon-pair generation rates N. Values of the photon-pair generation rate N decrease

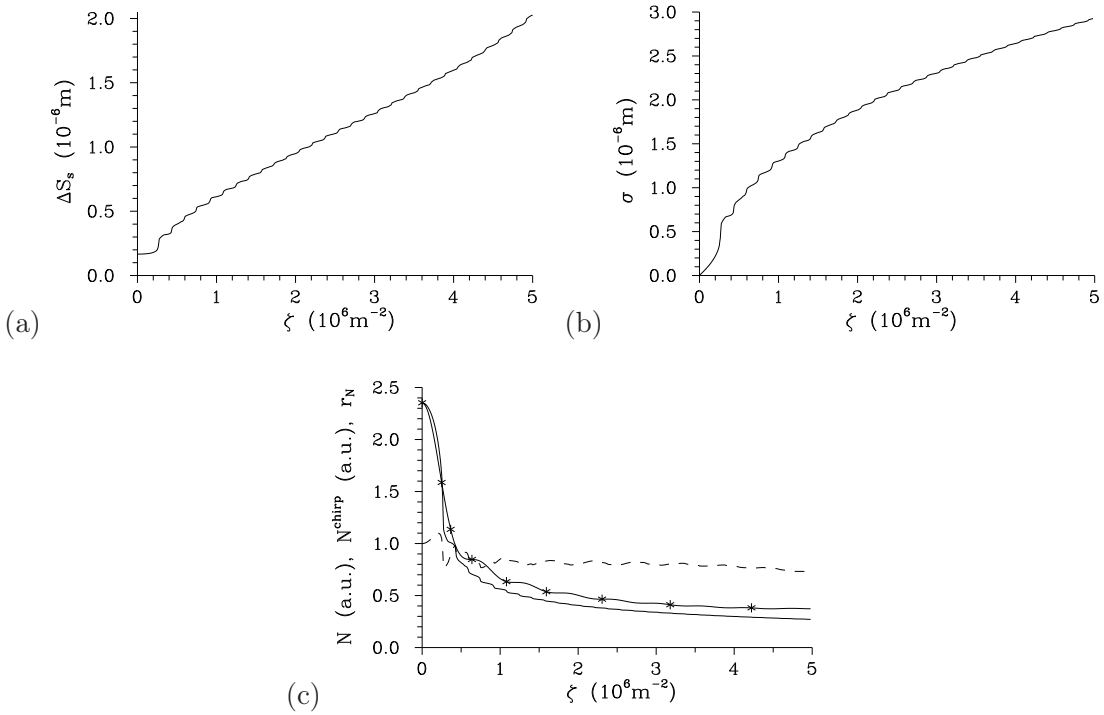

Figure 5.4: (a) Signal-field spectral width ΔS_s (FWHM) as a function of chirping parameter ζ. (b) Transformation curve between the standard deviation σ and chirping parameter ζ assuming the same spectral widths ΔS_s. (c) Photon-pair generation rate for chirped (N^{chirp}, solid curve with $*$) and random (N, solid curve) structures and their ratio r_N ($r_N = N/N^{\text{chirp}}$, dashed curve) as functions of chirping parameter ζ; $N_L = 700$.

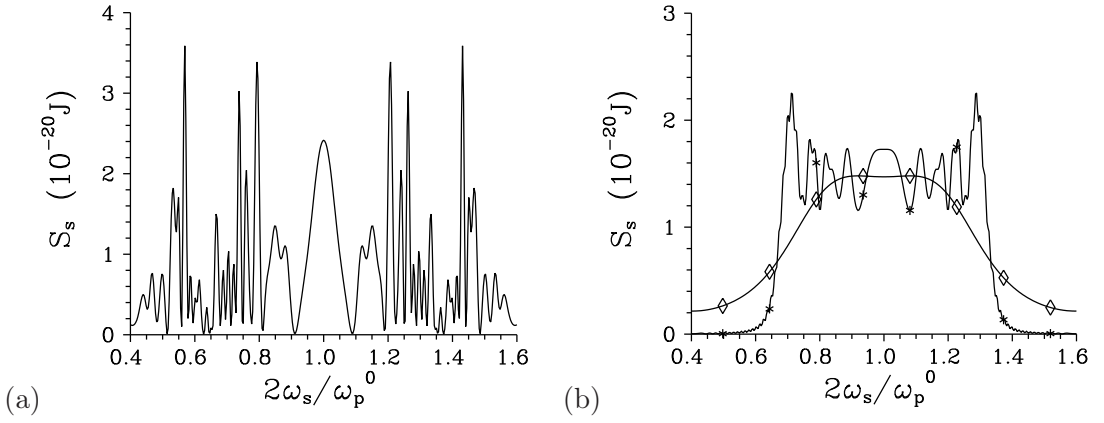

Figure 5.5: Signal-field spectrum S_s for (a) one typical realization of RPS (solid curve) and (b) CPPS (solid curve with $*$) and an ensemble of RPSs (solid curve with $\diamond$). Spectra S_s are normalized such that one photon is emitted; $\sigma = 2.1 \times 10^{-6}$m, $\zeta = 2.5 \times 10^6$m^{-2}, $N_L = 700$.

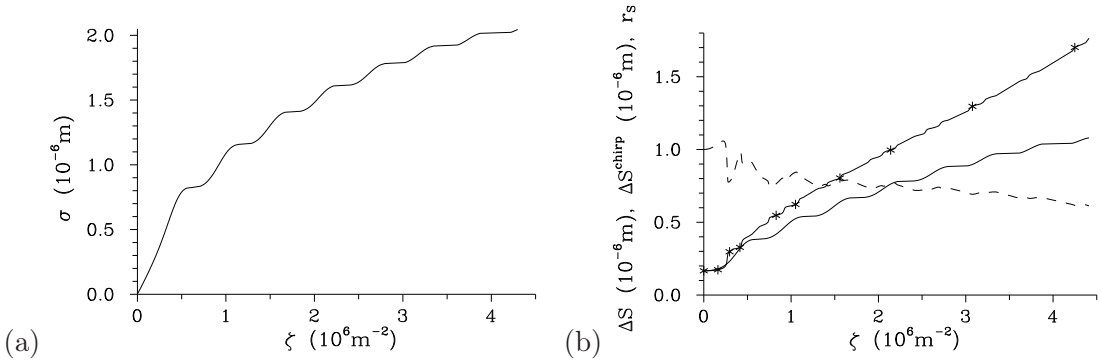

Figure 5.6: (a) Transformation curve between the standard deviation σ of RPSs and chirping parameter ζ assuming the same photon-pair generation rates N. (b) Signal-field spectral widths (FWHM) for random (ΔS_s, solid curve) and chirped ($\Delta S_s^{\rm chirp}$, solid curve with $*$) structures and their ratio r_S ($r_S = S_s/S_s^{\rm chirp}$, dashed curve) as functions of chirping parameter ζ; $N_L = 700$.

with the increasing values of chirping parameter ζ [see Fig. 5.4(c)]. Transformation curve between standard deviation σ and chirping parameter ζ stemming from the requirement of equal generation rates N is monotonous and is plotted in Fig. 5.6(a) in the considered case. The corresponding signal-field widths ΔS_s plotted in Fig. 5.6(b) reveal that CPPSs provide broader spectra for the most of values of chirping parameter ζ. However, the difference in spectral widths in CPPSs and RPSs is not dramatic.

5.4 Temporal Correlations, Entanglement Time

Since we assume cw-pumping with amplitude ξ_p at frequency ω_p^0, i.e. $E_p^{(+)}(\omega_p) = \xi_p \delta(\omega_p - \omega_p^0)$, formulas in Eqs. (3.35) and (3.36) can be simplified in this case and recast into the following form:

$$\begin{aligned}\rho(\tau) &= \frac{\hbar^2}{8\epsilon_0^2 c^2 \mathcal{B}^2}\frac{|\xi_p|^2}{R_0}\mathrm{Re}\Bigg[\exp(i\omega_p^0\tau)\int_0^\infty d\omega_s \omega_s(\omega_p^0-\omega_s)|g(\omega_s,\omega_p^0-\omega_s)|^2 \\ &\quad \times \exp(-2i\omega_s\tau)\mathcal{F}\left(\Delta k(\omega_s,\omega_p^0-\omega_s),\Delta k(\omega_p^0-\omega_s,\omega_s)\right)\Bigg], \qquad (5.8)\\ R_0 &= \frac{\hbar^2|\xi_p|^2}{8\epsilon_0^2 c^2\mathcal{B}^2}\int_0^\infty d\omega_s\omega_s(\omega_p^0-\omega_s)|g(\omega_s,\omega_p^0-\omega_s)|^2 \\ &\quad \times\left|\mathcal{F}\left(\Delta k(\omega_s,\omega_p^0-\omega_s),\Delta k(\omega_s,\omega_p^0-\omega_s)\right)\right|^2; \qquad (5.9)\end{aligned}$$

$g_0 \equiv g(\omega_s^0, \omega_i^0)$. Function $\mathcal{F}$ introduced in Eqs. (5.9) and (5.9) incorporates phase-matching conditions into the description of temporal properties of photon pairs and is defined according to the formula:

$$\mathcal{F}(\Delta k, \Delta k') = \langle F(\Delta k) F^*(\Delta k') \rangle_{\rm av}; \tag{5.10}$$

phase-matching function F has been introduced in Eq. (3.26).

Considering RPSs with fluctuations of boundaries described by a Gaussian distribution in Eq. (3.24) function $\mathcal{F}$ in Eq. (5.10) takes the form:

$$\begin{aligned}
\mathcal{F}(\Delta k, \Delta k') &= \frac{4}{\Delta k \Delta k'} \tilde{\mathcal{F}}(\Delta k, \Delta k') \exp[-i(\Delta k - \Delta k') N_L l_0], & (5.11)\\
\tilde{\mathcal{F}}(\Delta k, \Delta k') &= \frac{1 - H(Dk)^{N_L+1}}{1 - H(Dk)} \Bigg[\frac{H(\Delta k)}{H(\Delta k) + H(Dk)} \\
&\quad \times \left(-H(\Delta k) \frac{1 - [-H(\Delta k)]^{N_L}}{1 + H(\Delta k)} - H(Dk) \frac{1 - [H(Dk)]^{N_L}}{1 - H(Dk)} \right) \\
&\quad + \big(\Delta k \longleftrightarrow -\Delta k'\big) \Bigg]; & (5.12)
\end{aligned}$$

$Dk = \Delta k - \Delta k'$. Function H occurring in Eq. (5.12) has been defined in Eq. (5.2). Symbol $(\Delta k \longleftrightarrow -\Delta k')$ in Eq. (5.12) replaces the term that is obtained by the indicated exchange applied to the preceded term inside the brackets.

Considering 'weakly-random' structures, the following form of the function $\tilde{\mathcal{F}}$ can be derived:

$$\begin{aligned}
\tilde{\mathcal{F}}^{\rm w-r}(\Delta k, \Delta k') &= G(Dk) \frac{1 - \exp[iDkl_0(N_L+1)]}{1 - \exp(iDkl_0)} \\
&\quad + \Bigg[\frac{G(\Delta k) G(\Delta k')}{1 - \exp(-i\Delta k' l_0)} \left(\frac{1 - \exp(i\Delta k N_L l_0)}{1 - \exp(-i\Delta k l_0)} + \frac{1 - \exp(-iDk N_L l_0)}{1 - \exp(-iDk l_0)} \right) \\
&\quad + \big(\Delta k \longleftrightarrow -\Delta k'\big) \Bigg]. & (5.13)
\end{aligned}$$

On the other hand, function $\tilde{\mathcal{F}}^{\rm chirp}$ attains a simple form in case of CPPSs:

$$\tilde{\mathcal{F}}^{\rm chirp}(\Delta k, \Delta k') = F^{\rm chirp}(\Delta k) F^{\rm chirp*}(\Delta k'), \tag{5.14}$$

where the formula for $F^{\rm chirp}$ is written in Eq. (5.6).

The general formula in Eq. (3.37) can be recast into the following form using the

expression for function $\mathcal{F}$ in Eq. (5.10):

$$
\begin{aligned}
I^{\mathrm{sum}}(\tau) \;=\; & \frac{\eta^{\mathrm{sum}}\hbar^2}{4\varepsilon_0^2 c^2 \mathcal{B}^2}\int_0^\infty d\omega_p |E_p^{(+)}(\omega_p)|^2 \\
& \int_0^\infty d\omega_s \sqrt{\omega_s(\omega_p-\omega_s)}\int_0^\infty d\omega_s' \sqrt{\omega_s'(\omega_p-\omega_s')} \\
& \times g(\omega_s,\omega_p-\omega_s) g^*(\omega_s',\omega_p-\omega_s')\exp[-i(\omega_s-\omega_s')\tau] \\
& \times \mathcal{F}\left(\Delta k(\omega_s,\omega_p-\omega_s),\Delta k(\omega_s',\omega_p-\omega_s')\right). \qquad (5.15)
\end{aligned}
$$

When deriving (5.15) we have assumed that the nonlinear medium in which sum-frequency generation occurs is ideally phase matched for frequencies present in the signal and idler fields.

A detailed analysis of the expression that gives the coincidence-count rate R_n in a Hong-Ou-Mandel interferometer reveals an important property: the rate R_n does not depend on phase variations along the signal- and idler-field spectra in cw regime. This property is frequently referred as nonlocal dispersion cancellation [78, 79]. It follows that entanglement time $\Delta\tau^{\mathrm{HOM}}$ is inversely proportional to spectral widths ΔS_s and ΔS_i of the signal and idler fields despite their complex profiles. We note that the entanglement time $\Delta\tau^{\mathrm{HOM}}$ is determined by a temporal extension (FWHM) of the coincidence-count interference pattern formed by the rate $R_n(\tau)$. Entanglement time $\Delta\tau^{\mathrm{HOM}}$ thus shortens with increasing values of the standard deviation σ for RPSs. The dependence of entanglement time $\Delta\tau^{\mathrm{HOM}}$ on the deviation σ for an ensemble of RPSs composed of 700 domains is shown in Fig. 5.7. We can see in Fig. 5.7 that entanglement times $\Delta\tau^{\mathrm{HOM}}$ can be as short as several fs for sufficiently large values of the deviation σ. This indicates that temporal quantum correlations can be confined into an interval characterizing one optical cycle provided that spectral phase variations in the signal and idler fields are compensated. Entanglement times $\Delta\tau^{\mathrm{HOM}}$ of CPPSs with the same signal-field spectral widths ΔS_s are plotted in Fig. 5.7 for comparison that reveals nearly identical entanglement times of both types of structures.

Typical coincidence-count interference patterns given by R_n for photon pairs generated in both types of structures are compared in Fig. 5.8. They demonstrate a close similarity of photon-pair behavior in a Hong-Ou-Mandel interferometer. There occur typical oscillations at the shoulders of the interference dips. Whereas regular oscillations characterize CPPSs, irregular oscillations with larger amplitudes occur for individual realizations of RPSs. However, widths of interference dips remain practically unchanged for different realizations of RPSs.

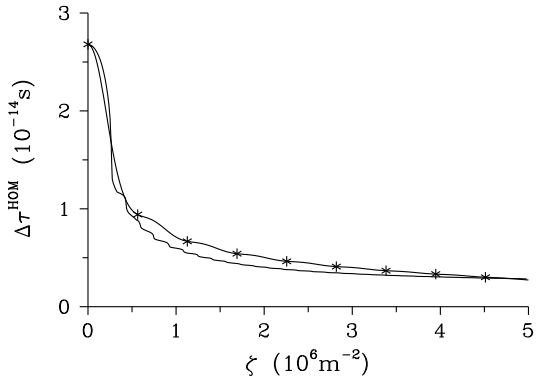

Figure 5.7: Entanglement time $\Delta\tau^{\mathrm{HOM}}$ (FWHM) as a function of chirping parameter ζ for an ensemble of RPSs with standard deviations σ derived from the curve in Fig. 5.4b (solid curve) and CPPSs (solid curve with $*$); $N_L = 700$.

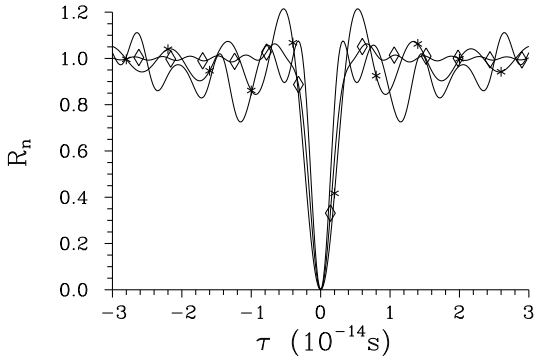

Figure 5.8: Coincidence-count rate R_n as it depends on relative time delay τ for one realization of RPS (solid curve), CPPS (solid curve with $*$), and an ensemble of RPSs (solid curve with $\diamond$); $\sigma = 2.1 \times 10^{-6}\mathrm{m}$, $\zeta = 2.5 \times 10^{6}\mathrm{m}^{-2}$, $N_L = 700$.

Correlation times $\Delta\tau^{\mathrm{sum}}$ emerging from sum-frequency generation are in general longer than entanglement times $\Delta\tau^{\mathrm{HOM}}$ observed in a Hong-Ou-Mandel interferometer because of a strong phase modulation along the wide signal- and idler-field spectra S_s and S_i (see Fig. 5.9).

Correlation times $\Delta\tau^{\mathrm{sum}}$ can be even an order of magnitude greater compared to entanglement times $\Delta\tau^{\mathrm{HOM}}$ for structures with ultra-broadband spectra. However, phase modulation along the spectrum can be compensated to certain extent which gives shorter correlation times $\Delta\tau^{\mathrm{sum}}$. CPPSs have more regular spectral phase behavior (as demonstrated in Fig. 5.9) and quadratic phase compensation is usually sufficient to provide wave-packets several fs long. As for individual realizations of RPSs, quadratic

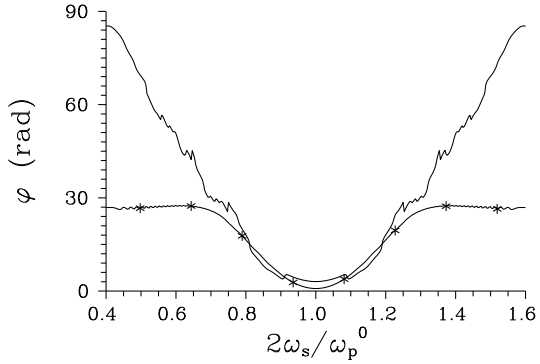

Figure 5.9: Phase φ of the two-photon spectral amplitude $\Phi(\omega_s, \omega_p^0 - \omega_s)$ as it depends on normalized signal-field frequency $2\omega_s/\omega_p^0$ for one realization of RPS (solid curve) and CPPS (solid curve with $*$); $\sigma = 2.1 \times 10^{-6}$m, $\zeta = 2.5 \times 10^{6}\mathrm{m}^{-2}$, $N_L = 700$.

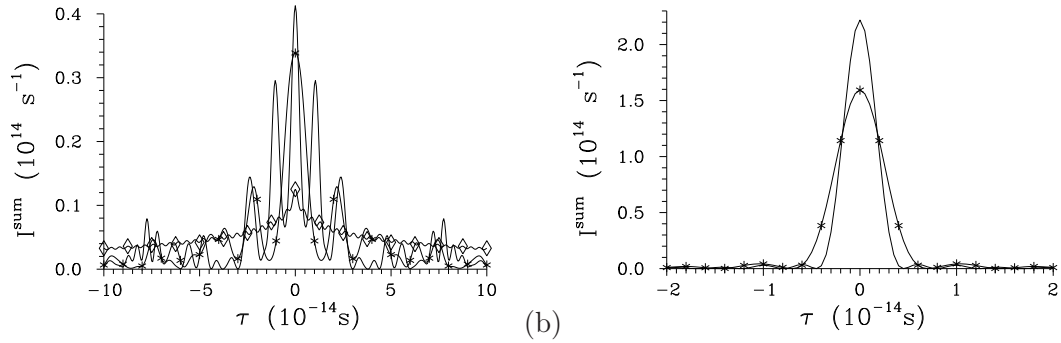

Figure 5.10: Sum-frequency field intensity I^{sum} as a function of relative time delay τ for one realization of RPS (solid curve), CPPS (solid curve with $*$), and an ensemble of RPSs (solid curve with $\diamond$). In (a) quadratic chirp in the signal-field amplitude spectrum is compensated for one realization of RPS and CPPS; in (b) complete spectral phase compensation is assumed. The curves are normalized such that $\int_{-\infty}^{\infty} d\tau I^{\mathrm{sum}}(\tau) = 1$; $\sigma = 2.1 \times 10^{-6}$m, $\zeta = 2.5 \times 10^{6}\mathrm{m}^{-2}$, $N_L = 700$.

compensation is less efficient because of more irregular phase spectral behavior. Despite this values of temporal constants typical for chirped structures can be approached [see Fig. 5.10(a)]. Provided that an ideal phase compensation is reached, both types of structures give comparable results [see Fig. 5.10(b)] and are capable to generate photon pairs with wave-packets extending over the duration of one optical cycle. Experimentally, pulse shapers have been developed for this task and their capabilities in the area of photon pairs have already been demonstrated [80]. Comparison of the results ob-

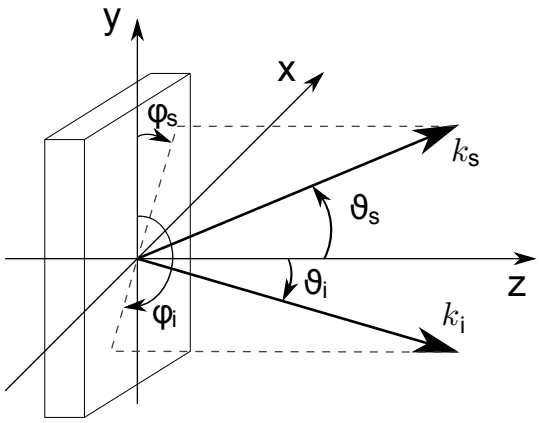

Figure 5.11: Geometric scheme for the description of spatial properties. Direction of the signal- (idler-) field wave vector k_s (k_i) is given by radial ϑ_s (ϑ_i) and azimuthal φ_s (φ_i) emission angles.

tained with quadratic and ideal compensations reveals that correlation times $\Delta\tau^{\mathrm{sum}}$ are approx. two times larger if we restrict ourselves to quadratic compensation. Also the value of quadratic chirp that needs compensation differs for individual realizations of RPS. This requires an adaptive phase compensator. On the other hand phase compensation in case of CPPS can be reached in a simpler way, e.g., by inserting a peace of suitable material of defined length [81, 82]. Despite this RPSs are challenging both for basic physical experiments as well as metrology applications.

5.5 Correlations in the Transverse Plane

In order to describe spatial properties of the signal and idler beams (in the transverse plane) a simple generalization of Eq. (3.21) is needed. The inclusion of phase-matching conditions also in the directions along the x and y axes and assumption of spectrally-flat transverse pump-beam profile $E_{p\perp}(x, y)$ result in the following separable form of a two-photon spectral amplitude Φ that additionally depends on radial (ϑ_s, ϑ_i) and azimuthal (φ_s, φ_i) signal- and idler-field emission angles (see Fig. 5.11):

$$\Phi(\omega_s, \omega_i, \vartheta_s, \varphi_s, \vartheta_i, \varphi_i) \;=\; \Phi_z(\omega_s, \omega_i, \vartheta_s, \varphi_s, \vartheta_i, \varphi_i)\Phi_{xy}(\omega_s, \omega_i, \vartheta_s, \varphi_s, \vartheta_i, \varphi_i), \tag{5.16}$$

where function Φ_z arises from phase-matching conditions in the z direction and function Φ_{xy} originates in phase-matching conditions in the transverse xy plane (see Fig. 5.11).

Function Φ_z can be derived in analogy with the formula in Eq. (3.21):

$$\Phi_z(\omega_s,\omega_i,\vartheta_s,\varphi_s,\vartheta_i,\varphi_i) \;=\; g(\omega_s,\omega_i)E_p^{(+)}(\omega_s+\omega_i)F(\Delta k(\omega_s,\omega_i,\vartheta_s,\varphi_s,\vartheta_i,\varphi_i)), \tag{5.17}$$

where the stochastic function F has been introduced in Eq. (3.22). Phase-matching conditions in the xy plane give the function Φ_{xy} the following form:

$$\Phi_{xy}(\omega_s,\omega_i,\vartheta_s,\varphi_s,\vartheta_i,\varphi_i) \;=\; \int_{-\infty}^{\infty}dx\int_{-\infty}^{\infty}dyE_{p\perp}(x,y)\exp\left(i\Delta k_x x+i\Delta k_y y\right) \tag{5.18}$$

that includes a pump-beam amplitude profile $E_{p\perp}(x,y)$ in the transverse plane. Assuming normal incidence of the pump beam, the cartesian components of nonlinear phase mismatch in Eqs. (5.17) and (5.18) can be written as:

$$\begin{aligned}
\Delta k_x &= k_s(\omega_s)\sin(\vartheta_s)\sin(\varphi_s)+k_i(\omega_i)\sin(\vartheta_i)\sin(\varphi_i)\\
\Delta k_y &= k_s(\omega_s)\sin(\vartheta_s)\cos(\varphi_s)+k_i(\omega_i)\sin(\vartheta_i)\cos(\varphi_i)\\
\Delta k_z &= k_p(\omega_s+\omega_i)-k_s(\omega_s)\cos(\vartheta_s)-k_i(\omega_i)\cos(\vartheta_i).
\end{aligned} \tag{5.19}$$

We assume a Gaussian pump-beam transverse profile in numerical calculations:

$$E_{p\perp}(x,y)=\frac{1}{\pi\Delta x_p\Delta y_p}\exp\left(-\frac{x^2}{\Delta x_p^2}-\frac{y^2}{\Delta y_p^2}\right), \tag{5.20}$$

Δx_p (Δy_p) stands for the pump-beam width along the x (y) direction.

We first pay attention to transverse properties of the signal beam only. Its spectral density s_s defined as

$$s_s(\omega_s,\vartheta_s,\varphi_s) \;=\; \sin(\vartheta_s)\int d\omega_i\int d\vartheta_i\sin(\vartheta_i)\int d\varphi_i|\Phi(\omega_s,\omega_i,\vartheta_s,\varphi_s,\vartheta_i,\varphi_i)|^2 \tag{5.21}$$

depends on the signal-field radial (ϑ_s) and azimuthal (φ_s) emission angles. As we study photon-pair emission near the collinear geometry, the signal beam (as well as the idler beam) has rotational symmetry along the z axis. The dependence of spectral density s_s on signal-field radial emission angle ϑ_s is shown in Fig. 5.12. Investigating one realization of RPS we observe a typical 'strip-like' behavior depicted in Fig. 5.12(a). Fixing the value of radial emission angle ϑ_s spectrum $s_s(\omega_s)$ is composed of many peaks

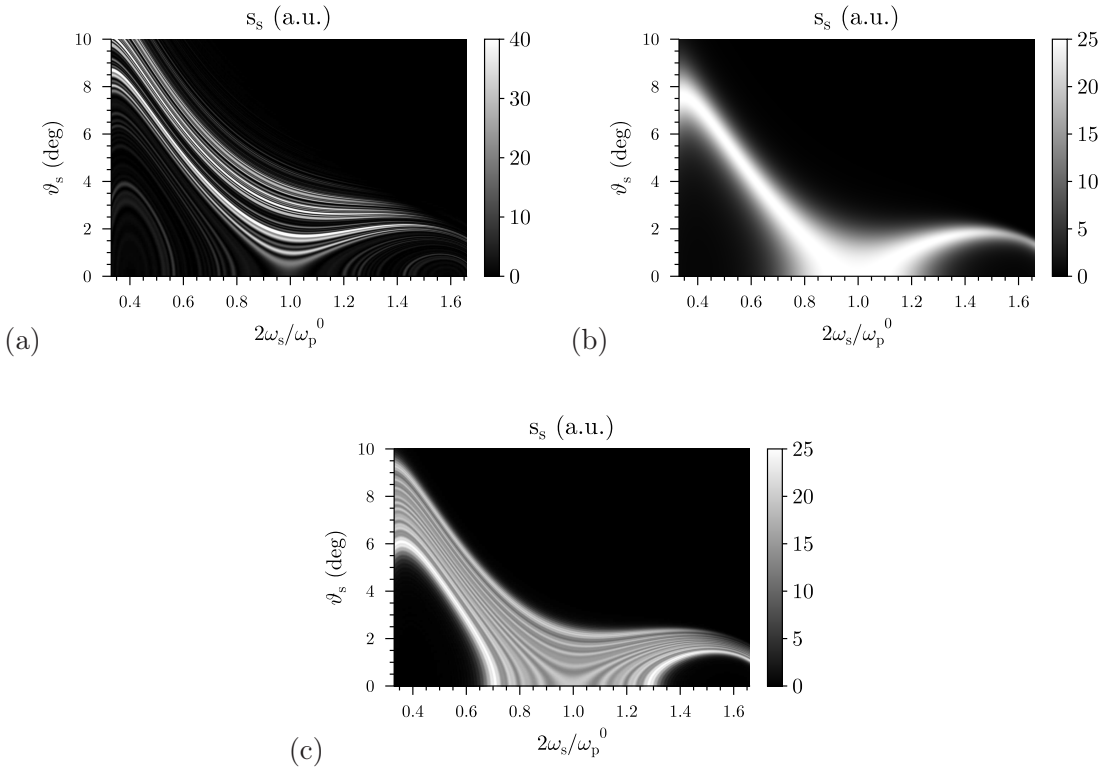

Figure 5.12: Map of signal-field spectral density s_s as it depends on signal-field radial emission angle ϑ_s for (a) one realization of RPS, (b) an ensemble of RPSs, and (c) CPPS; $\varphi_s = 0$ deg, $\sigma = 2.1 \times 10^{-6}$m, $\zeta = 2.5 \times 10^{6}\mathrm{m}^{-2}$, $N_L = 700$.

occurring at positions specific for the studied realization [compare also with Fig. 5.5(a)]. Each peak changes continuously its central frequency as the radial emission angle ϑ_s moves. We note that this is typical also for layered structures that form band gaps [83]. Averaging over many realizations of RPSs smoothes this 'strip-like' behavior [see Fig. 5.12(b)] and leads to that resembling CPPSs [compare Figs. 5.12(b) and 5.12(c)]. In these cases spectral splitting is observed [84]. This behavior originates in phase-matching conditions along the z direction.

Integration of spectral densities s_s over the signal-field frequency ω_s gives us densities n_s of photon-pair numbers that are plotted in Fig. 5.13 for the structures studied in Fig. 5.12. Whereas the profile of density $n_s(\vartheta_s)$ is complex for one realization of RPS, typical shapes with one maximum around a nonzero value of ϑ_s characterize the profiles of density $n_s(\vartheta_s)$ for an ensemble of RPSs and CPPS.

Correlated area g_i of an (idler) photon in a pair represents spatial analogy to entanglement time and characterizes correlations of photon twins in the transverse plane.

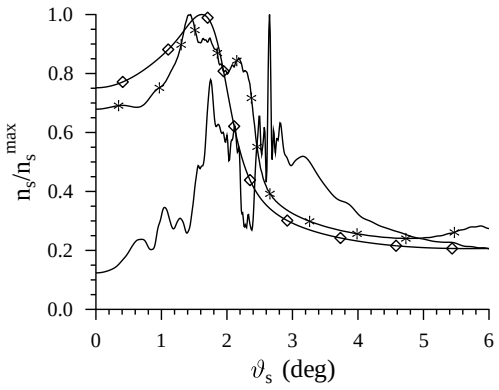

Figure 5.13: Profile of density n_s of signal-field photon numbers as a function of signal-field radial emission angle ϑ_s for one realization of RPS (solid curve), CPPS (solid curve with $*$), and an ensemble of RPSs (solid curve with $\diamond$); $n_s^{\max} = \max_{\vartheta_s}[n_s(\vartheta_s)]$. Plane-wave pumping is assumed; $n_s(\vartheta_s, \psi_s) = \int d\omega_s s_s(\omega_s, \vartheta_s, \varphi_s)$; $\varphi_s = 0$ deg, $\sigma = 2.1 \times 10^{-6}$m, $\zeta = 2.5 \times 10^6 \mathrm{m}^{-2}$, $N_L = 700$.

By definition, it gives probability of emitting an idler photon into radial emission angle ϑ_i and azimuthal emission angle φ_i provided that its signal twin has been emitted in a fixed radial emission angle ϑ_s and azimuthal emission angle φ_s, i.e.:

$$g_i(\vartheta_i, \varphi_i; \vartheta_s, \varphi_s) = \sin(\vartheta_s)\sin(\vartheta_i) \int d\omega_s \int d\omega_i |\Phi(\omega_s, \omega_i, \vartheta_s, \varphi_s, \vartheta_i, \varphi_i)|^2. \qquad (5.22)$$

Because we mainly pay attention to beams propagating in the vicinity of the z axis, we assume that the signal photon is emitted along the z axis ($\vartheta_s = \varphi_s = 0$ deg). The correlated area as described by function g_i in Eq. (5.22) then has rotational symmetry and its profiles along the radial emission angle ϑ_i for CPPS and an ensemble of RPSs nearly coincide, as documented in Fig. 5.14(a). On the other hand, broader profiles are typical for individual realizations of RPSs. These individual realizations form compact correlated areas without large local peaks (compare with Fig. 5.5 where spectrum S_s for one realization of RPS is plotted). The width $\Delta\vartheta_i$ of the correlated area along the radial angle ϑ_i depends in general on phase-matching conditions along the z and ϑ_i axes. Thus length of the structure, pump-field (temporal) spectral width as well as width of the pump-beam waist determine together the width $\Delta\vartheta_i$ (for more details, see [84]). For example, focusing the pump beam, values of the radial width $\Delta\vartheta_i$ can be varied nearly by one order of magnitude [see Fig. 5.14(b)]. This behavior can be easily explained by

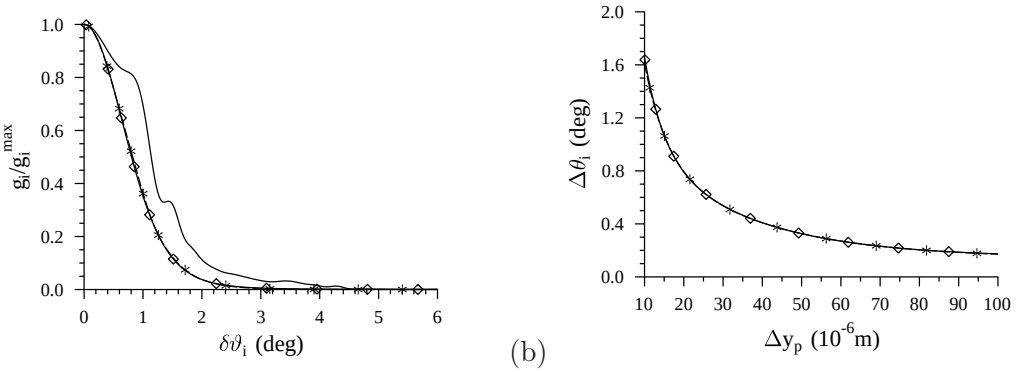

Figure 5.14: (a) Radial profile $g_i(\vartheta_i)$ of the correlated area for $\Delta y_p = 1 \times 10^{-5}$m and (b) radial width $\Delta\vartheta_i$ of the correlated area as it depends on pump-beam width Δy_p for one realization of RPS (solid curve), CPPS (solid curve with $*$), and an ensemble of RPSs (solid curve with $\diamond$); $\vartheta_i = \vartheta_i^0 + \delta\vartheta_i$; $g_i^{\max} = \max_{\vartheta_i}[g_i(\vartheta_i)]$. Radially symmetric pump beam is assumed, i.e. $\Delta x_p = \Delta y_p$; $\varphi_s = \vartheta_s = 0$ deg, $\varphi_i = 180$ deg, $\vartheta_i^0 = 0$ deg; $\sigma = 2.1 \times 10^{-6}$m, $\zeta = 2.5 \times 10^6 \mathrm{m}^{-2}$, $N_L = 700$.

the fact that the more the pump beam is focused, the wider its spatial spectrum in the transverse plane, and so the weaker the phase-matching conditions in this plane.

5.6 The Role of Temperature

We have seen that an ensemble of randomly poled structures and a chirped periodically poled structure have similar properties. This close similarity is preserved also when studying temperature dependencies [76] that are in general weak. On the other hand, behavior of individual realizations of RPSs manifests a stronger temperature dependence. However, influence of temperature varies from realization to realization. Whereas properties of the realization of RPS studied above do not considerably change with temperature (see Fig. 5.15 for the signal-field spectral width ΔS_s in the temperature range from 284 to 300 K), other realizations are more prone to the change of temperature. This can be conveniently used for efficient temperature modifications of properties of photon pairs. We note that these effects have their origin in temperature dependence of indexes of refraction [76].

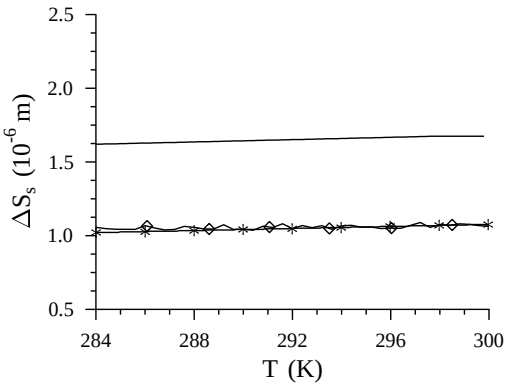

Figure 5.15: Signal-field spectral width ΔS_s as it depends on temperature T for one realization of RPS (solid curve), CPPS (solid curve with $*$), and an ensemble of RPSs (solid curve with $\diamond$); $\sigma = 2.1 \times 10^{-6}$m, $\zeta = 2.5 \times 10^{6}$m^{-2}, $N_L = 700$.

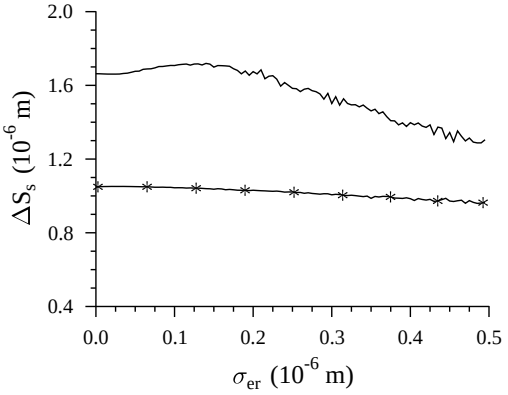

Figure 5.16: Signal-field spectral width ΔS_s as a function of variance $\sigma_{\rm er}$ of the fabrication error for one realization of RPS (solid curve) and CPPS (solid curve with $*$). Averaging over the fabrication error was done in 1000 randomly chosen positions; $\sigma = 2.1 \times 10^{-6}$m, $\zeta = 2.5 \times 10^{6}$m^{-2}, $N_L = 700$.

5.7 The Role of Small Random Fabrication Errors

In the fabrication process, a small random error necessarily occurs [57]. This error is sometimes called a duty cycle error and, in general, leads to lowering of photon-pair emission rates [69]. Considering spectral widths, they are resistant against this error in uniformly periodically-poled crystals [57] [see also Eq. (5.5) valid for 'weakly-random'

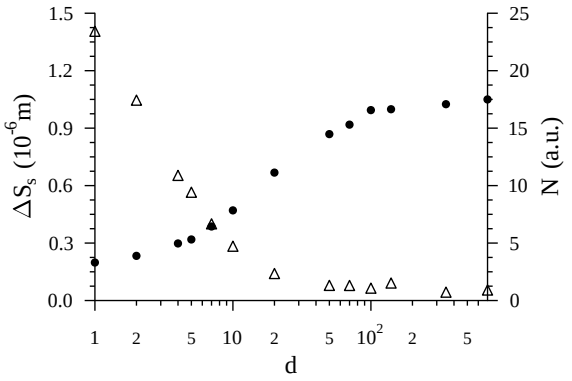

Figure 5.17: Signal-field spectral width ΔS_s (solid curve with $\bullet$) and photon-pair generation rate N (solid curve with $\triangle$) as functions of segment length d. Averaging over 1000 random positions of segments was used in calculations. $\zeta = 2.5 \times 10^6 \mathrm{m}^{-2}$, $N_L = 700$.

structures]. On the other hand, spectral widths are slightly reduced in CPPSs as documented in Fig. 5.16. We can see in Fig. 5.16 that a (large) fabrication error with variance $\sigma_{\mathrm{er}} = 5 \times 10^{-7}\mathrm{m}$ results in the reduction of signal-field spectral width ΔS_s only by approx. 10 %. Individual realizations of RPSs are much more sensitive to the fabrication error. The observed spectral changes depend on individual realizations. As an example, the signal-field spectral width ΔS_s of the sample analyzed above decreases with the increasing variance σ_{er} of the fabrication error. This is natural, because spectrum of this realization is broader compared to the ensemble mean value. We note that it holds also here that the narrower the signal-field spectrum, the greater the photon-pair generation rate N and vice versa.

5.8 The Role of Ordering in Chirped Periodically-Poled Structures

The benefit of ordering of individual domains by their lengths in a chirped periodically poled structure can be quantified as follows. We take an ordered structure and divide it into segments containing d domains. We then randomly position these segments in a new artificial structure and finally obtain mean values of physical quantities after averaging over random positions. In the limiting case of $d = 1$ we have a completely random structure similar to those studied above. It can be shown that the signal-field spectral width ΔS_s decreases with the decreasing segment length d (see Fig. 5.17). This

is accompanied by an increase of photon-pair generation rate N. This behavior reflects the fact that spectra of the fields coming from individual domains are combined in a more constructive way in the central spectral area with the increasing randomness (decreasing value of segment length d).

The graph in Fig. 5.17 also demonstrates that the requirement for the same spectral widths ΔS_s of RPSs and CPPS inevitably implies that the histogram of domains' lengths for RPSs is broader than that obtained for CPPS.

Chapter 6

Higher-Multiple Orders of Stochastic Quasi-Phase-Matching of Randomly Poled Crystals

6.1 Introduction

In this chapter, we extend the previous study to the higher-multiple orders of SQPM. As we want to include all orders of SPQM, we express random lengths l of domains in the form $l = Zl_0 + \delta l$, where Z is a positive real number giving the order of SQPM. The optimum length l_0 of domains is derived from the natural phase mismatch Δk of the central wave vectors ($l_0 = \pi/\Delta k$). Randomness in domains' positions is described by declinations δl with a Gaussian probability distribution as defined in Eq. (3.24) in section 3.3. For numerical modelling, we consider a 5-mm long $LiNbO_3$ crystal with an optical axis parallel to the boundaries in Type-0 collinear configuration (all extraordinary photons are vertically polarized). The crystal is pumped by a monochromatic plane wave at the wavelength $\lambda_{p0} = 400$ nm. The signal and idler photons are chosen to have the same central wavelengths $\lambda_{s0} = \lambda_{i0} = 800$ nm. The optimum length l_0 of domains equals 1.2839 μm in this configuration. The average amount of layers under these circumstances is equal to 3895.

6.2 Photon-Pair Rates

High numbers N of generated photon pairs occur when Z is an odd integer [see Fig. 6.1(a)], as expected for a rectangular shape of the nonlinear modulation [57]. In these cases, we

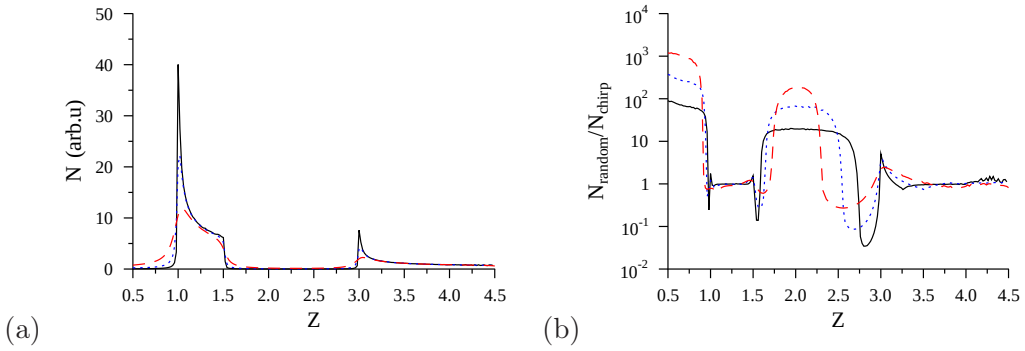

Figure 6.1: (a) Averaged number N of generated photon pairs and (b) ratio $N_{\text{random}}/N_{\text{chirp}}$ of photon-pair numbers generated from randomly poled and chirped periodically poled crystals for the same width ΔS_s as functions of Z for $\sigma = 0.1$ μm (solid black curve), 0.2 μm (dotted blue curve) and 0.4 μm (dashed red curve). Averaged over 100 samples.

observe Z-th-order SQPM. However, appreciable numbers N of generated photon pairs are found also for values of Z larger than these optimum values. A closer inspection of spectra shows that the structure allows for QPM at non-degenerate signal and idler frequencies [see Fig. 6.3(d)] in these areas. If the value of Z is such that no QPM is possible, the numbers N of generated photon pairs are very low. The numbers N of photon pairs also decrease with increasing values of deviation σ for values of Z allowing QPM ($Z \approx 1, 3$). On the other hand, the numbers N of photon pairs increase with increasing values of σ provided that no QPM is reached.

Large numbers N of photon pairs generated in randomly poled crystals are comparable to those characterizing chirped periodically-poled crystals [A1] widely used as sources of spectrally broad-band SPDC. Achievable numbers N of generated photon pairs make the third-order SQPM viable, even though the number N of generated photon pairs is approx. 10 times smaller compared to those characterizing first-order SQPM [see fig. 6.1(b)]. As chirped crystals have domains of different lengths ordered, more regular interference of light coming from individual domains occurs and leads to more regular spectral shapes. This favors chirped crystals for interferometric experiments.

6.3 Spectral Properties

Signal- and idler-field spectra are typically composed of many sharp peaks originating in complex interference of irregular fields' contributions coming from different do-

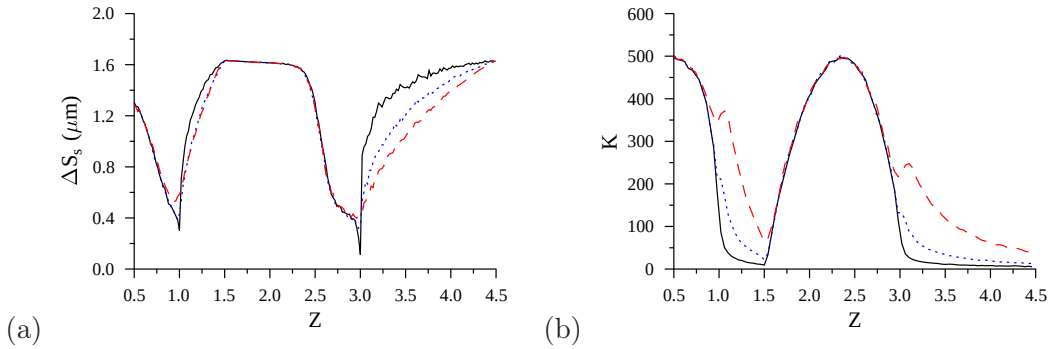

Figure 6.2: (a) Signal-field spectral width δS_s (FWHM) and (b) Schmidt number K as functions of Z for $\sigma = 0.1$ μm (solid black curve), 0.2 μm (dotted blue curve) and 0.4 μm (dashed red curve). Averaged over 100 samples.

mains (see Fig. 6.3 below). These peaks are localized in the spectral regions allowing QPM. If no QPM is possible, peaks are randomly distributed over a wide spectral area [see Fig. 6.3(b)]. The narrowest spectra are observed for odd integer values of Z [see Fig. 6.2(a)] and low values of deviation σ. The graph in Fig. 6.2(a) shows that, for a given value of deviation σ, considerably narrower signal-field spectra S_s are found for third-order SQPM in comparison with first-order SQPM ($\Delta S_s = 0.129$ μm versus $\Delta S_s = 0.309$ μm for $\sigma = 0.1$ μm). This can be explained by relatively smaller fluctuations of domains' lengths for third-order SQPM (the average domains' length equals $3l_0$). Whereas the signal-field spectral width ΔS_s increases with increasing values of deviation σ for values of Z allowing spectrally degenerate QPM, it decreases for values of Z suitable for spectrally non-degenerate QPM [see Fig. 6.2(a)]. Values of the signal-field spectral width ΔS_s can be widely changed by controlling randomness. For example, an increase of ΔS_s from 0.129 μm to 0.462 μm, i.e. more than three times, is reached by increasing the variance σ from 0.1 μm to 0.4 μm.

Photon pairs generated in random crystals also exhibit large amount of spectral entanglement due to their wide spectra as it has been revealed via the Schmidt decomposition defined by Eq. (2.3). The Schmidt number K (Eq. (2.8) gives about 200 independent paired modes in the signal-field spectrum S_s both for first-order and third-order SQPM [see Fig. 6.2(b)]. This is a consequence of both wide spectra and their complex structure. This makes the generated paired fields prospective for quantum information protocols based on complex entangled fields. We note that the number K of independent modes considerably decreases when spectrally non-degenerate QPM is reached. In this case, the number K of modes increases with increasing values of

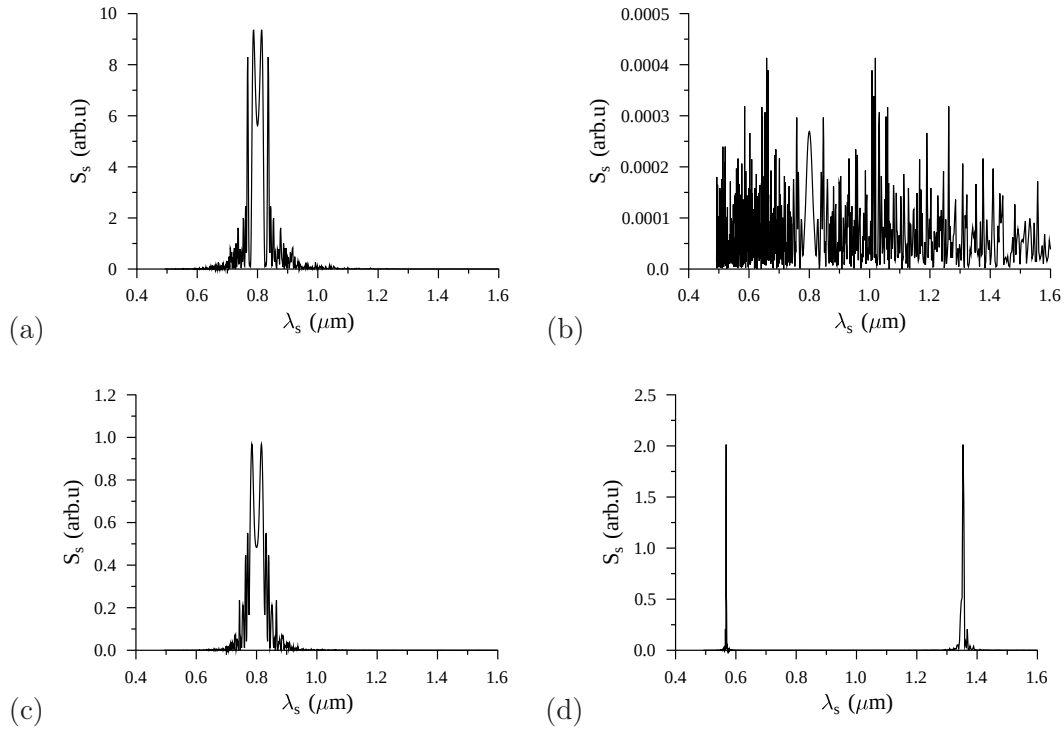

Figure 6.3: Signal-field spectrum S_s for one typical realization of the random structure with (a) $Z = 1$, (b) $Z = 2.5$, (c) $Z = 3$, and (d) $Z = 3.5$; $\sigma = 0.1$ μm.

variance σ [see Fig. 6.2(b)].

6.4 Temporal Properties

Entanglement time $\Delta\tau$ can be determined from the width of coincidence-count pattern R_n in a Hong-Ou-Mandel interferometer (see section 3.4) that gives the normalized number of coincidences as a function of mutual delay τ between the signal and idler photons. The simplified expression of rate R_n is obtained using Eqs. (3.32), (3.33) and (3.34) in the form:

$$R_n(\tau) = 1 - \frac{1}{R_0} \int d\omega_s \exp\left[-i\tau(\omega_{p0} - 2\omega_s)\right] \langle |F\left[\Delta k(\omega_s, \omega_{p0} - \omega_s)\right]|^2 \rangle_{av}, \qquad (6.1)$$

where $R_0 = \int d\omega_s \langle |F[\Delta k(\omega_s, \omega_{p0} - \omega_s)]|^2 \rangle_{av}$. The graph in Fig. 6.4 confirms that random crystals generate photon pairs with temporal correlations at fs time scale for all values of Z. Whereas 8-fs long entanglement time $\Delta\tau$ is found for first-order SQPM, $\Delta\tau = 12$ fs

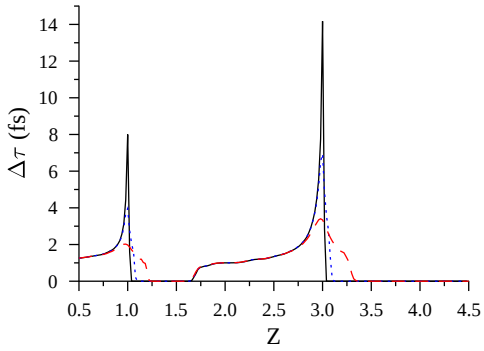

Figure 6.4: Entanglement time $\Delta\tau$ as functions of Z for $\sigma = 0.1$ μm (solid black curve), 0.2 μm (dotted blue curve) and 0.4 μm (dashed red curve). Averaged over 100 samples.

arises from third-order SQPM. These values even decrease when stronger randomness is applied. It holds in general that the wider the signal-field spectrum S_s the shorter the entanglement time $\Delta\tau$ [compare Fig. 6.2(a) and Fig. 6.4]. We note that the above considered entanglement time does not characterize temporal amplitude correlations that are much wider because of phase modulation along the spectra shown in Fig. 6.3. Nevertheless, spectral phase modulation can be compensated to some extent and signal and idler pulses long several tens of fs can be reached.

Chapter 7

Conclusion

In this thesis a systematic study of important characteristics of photon pairs generated in the process of spontaneous parametric down-conversion occurring in randomly poled non-linear crystals has been given. Photon-pair sources based on this process form nowadays an indispensable part of many experimental implementations of various entanglement-based quantum measurements, computing and communication methods. Randomly poled structures have been shown to be an inexpensive source of photon pairs with properties comparable to those coming from ordered nonlinear structures.

In more detail, we have investigated properties of photon pairs generated in randomly poled $LiNbO_3$ crystals. We have shown that the number of emitted photon pairs per second depends linearly on the number of layers. Increasing randomness of poling effectively reduces efficiency of the process considering a preselected finite spectral interval. Considering structures with the largest possible randomness widths of emitted photon spectra increase with the randomness. If restricted randomness is applied like in the considered case of weakly-random structures (disorder is applied to ordered boundaries of domains) only decrease of the production efficiency is observed with the increasing randomness. The band-width of emitted photons remains unchanged. A close similarity in properties of photon pairs coming from the randomly poled structures and linearly chirped poled structures has been revealed. Even certain mapping curves between parameters of random and chirped structures have been obtained. Temporal correlations between the signal and idler fields including entanglement times can be as short as a few femtoseconds in highly randomized structures, which allows temporal high-precision measurements. Spatial distributions of emitted photon fields as well as correlation areas have been shown to be similar for random, chirped and even individual realizations of random structures. Limitations of temperature tuning of the

phase-matching conditions have been revealed. The influence of fabrication errors has been quantified. The role of disorder in otherwise ordered linearly chirped periodically poled structures has been understood.

Also higher-order stochastic quasi-phase-matching has been investigated. Third-order stochastic quasi-phase-matching reached in randomly poled nonlinear crystals has been found useful for the generation of photon pairs. Despite its lower generation efficiency in comparison with first-order stochastic quasi-phase-matching it provides sufficient photon-pair generation rates based on three times longer domain lengths. Longer domain lengths allow to considerably widen the area of materials and conditions in which quasi-phase-matching can be applied. Similarly as first-order stochastic quasi-phase-matching, third-order stochastic quasi-phase-matching allows to generate spectrally ultra-wide photon pairs with temporal correlations at femtosecond scale. The generated photon pairs exhibit strong spectral entanglement arising from typically several hundred of independent paired modes present in the spectrum.

We have shown that randomly poled crystals with stochastic quasi-phase-matched spontaneous parametric down-conversion represent prospective sources of intense entangled photon pairs with low fabrication demands.

Stručné shrnutí v češtině

Tato práce představuje systematickou studii vlastností fotonových párů generovaných v procesu spontánní parametrické sestupné frekvenční konverze v náhodně pólovaných nelineárních krystalech. Fotonové zdroje založené na tomto procesu jsou dnes nepostradatelnou součástí mnoha experimentálních realizací kvantových metod měření, výpočtů a komunikace využívající kvantově provázané částice. Náhodně pólované nelineární struktury představují mezi těmito strukturami dostupné zdroje fotonových párů s vlastnostmi srovnatelnými s uspořádanými nelineárními strukturami.

Vlastnosti fotonových párů v náhodně pólovaných strukturách využívajících stochastického kvazi-fázového sladění jsou podrobně analyzovány na příkladu krystalů tvořených $LiNbO_3$. Je ukázáno, že počet emitovaných fotonových párů za jednu sekundu roste lineárně se vzrůstajícím počtem vrstev v krystalu. Počet emitovaných párů naopak klesá s rostoucí mírou neuspořádanosti vrstev v krystalu. Šířka emitovaných fotonových spekter roste s mírou náhodnosti struktury pro maximálně neuspořádané struktury. V případě uvažování neuspořádosti lokálního charakteru ovšem efektivita nelineárního procesu klesá s rostoucí náhodností struktury. Šířka spektra zůstává v tomto případě neměnná. Podobnost vlastností náhodně a lineárně čerpovaně uspořádaných pólovaných struktur je možné dokonce vyjádřit pomocí vztahů mezi parametry charakterizujícími oba typy struktur. Oba typy struktur generují fotonové páry s časovými korelacemi v řádech femtosekund. Fázové změny ve spektrech generovaných fotonových párů je možné zkompenzovat a tím využít tyto ultra-krátké časové korelace i v procesech založených na interferenci amplitud. Podobnost vlastností fotonových párů generovaných v náhodně a lineárně čerpovaně uspořádaných pólovaných strukturách byla nalezena i pro prostorové hustoty počtu fotonů a korelované plochy. Byla také vymezena oblast použitelnosti teplotní laditelnosti krystalů. Byl kvantifikován vliv výrobních chyb při pólovacím procesu. V neposlední řadě byl pochopen vliv uspořádání vrstev v lineárně čerpovaných uspořádaných strukturách.

Byly také uvažovány vyšší řády stochastického kvazi-fázového sladění. Třetí řád

stochastického kvazi-fázového sladění u krystalu $LiNbO_3$ je možné využít ve zdroji fotonových párů přes nižší efektivitu nelineárního procesu. Emise široko-spektrálních fotonových párů s extrémně krátkými časovými korelacemi v řádu femtosekund je pozorována i u tohoto třetího řádu stochastického kvazi-fázového sladění. Fotonové páry jsou typicky generovány do několika set nezávislých časo-prostorových módů, které mohou být využity při paralelním kvantovém zpracování informace těmito páry.

Náhodně pólované materiály tedy představují intenzívní zdroje kvantově-korelovaných fotonových párů s velkou výrobní tolerancí, které jsou považovány za perspektivní nástroj pro protokoly kvantového zpracování informace blízké budoucnosti.

List of author's publications

[A1] J. Svozilík and J. Peřina Jr., "Properties of entangled photon pairs generated in periodically poled nonlinear crystals," Phys. Rev. A **80**, 023819 (2009).

[A2] J. Svozilík and J. Peřina Jr., "Generation of entangled photon pairs in periodically poled nonlinear crystals," Proc. SPIE **7354**, 73540 (2009).

[A3] J. Svozilík and J. Peřina Jr., "Intense ultra-broadband down-conversion from randomly poled nonlinear crystals," Opt. Express **18**, 27130 (2010).

[A4] J. Perina Jr. and J. Svozilík, "Randomly poled crystals as a source of photon pairs," Phys. Rev. A **83**, 033808 (2011).

[A5] J. Svozilík, A. Valles, M. Hendrych, and J. P. Torres, "Bragg reflection waveguides as a source of photon pairs: theory and experiments," Proc. SPIE **8072**, 80720 (2011).

[A6] J. Svozilík, M. Hendrych, A. S. Helmy, and J. P. Torres, "Generation of paired photons in a quantum separable state in bragg reflection waveguides," Opt. Express **19**, 3115 (2011).

[A7] J. Svozilík and J. Peřina Jr., "Intense ultra-broadband down-conversion from randomly poled nonlinear crystals," Proc. SPIE **8071**, 807105 (2011).

[A8] J. Svozilík, M. Hendrych, and J. P. Torres, "Bragg reflection waveguide as a source of wavelength-multiplexed polarization-entangled photon pairs," Opt. Express **20**, 15015 (2012).

[A9] D. Javůrek, J. Svozilík, and J. Peřina Jr., "Entangled photon-pair generation in metallo-dielectric photonic bandgap structures," Proc. SPIE **8697**, 869727 (2012).

[A10] J. Svozilík, R. de Jesus Leon-Montiel, and J. P. Torres, "Implementation of a spatial two-dimensional quantum random walk with tunable decoherence," Phys. Rev. A **86**, 052327 (2012).

[A11] J. Svozilík, J. Peřina Jr, and J. P. Torres, "High spatial entanglement via chirped quasi-phase-matched optical parametric down-conversion," Phys. Rev. A **86**, 052318 (2012).

[A12] R. Machulka, J. Svozilík, J. Soubusta, J. Peřina Jr., and O. Haderka, "Spatial and spectral properties of the pulsed second-harmonic generation in a pp-ktp waveguide," Phys. Rev. A **87**, 013836 (2013).

[A13] J. Svozilík and J. Peřina Jr., "Higher-order stochastic quasi-phase-matching in spontaneous parametric down-conversion," submitted to Opt. Commun. .

[A14] R. de J. León-Montiel, J. Svozilík, L. J. Salazar-Serrano, and J. P. Torres, "Role of the spectral shape of quantum correlations in two-photon virtual-state spectroscopy," **accepted** for publication in New J. Phys. .

[A15] A. Valles, M. Hendrych, J. Svozilík, R. Machulka, P. Abolghasem, D. Kang, B. J. Bijlani, A. S. Helmy, and J. P. Torres, "Generation of polarization-entangled photon pairs in a bragg reflection waveguide," **accepted** for publication in Opt. Express .

Bibliography

[1] A. Einstein, B. Podolsky, and N. Rosen, "Can quantum-mechanical description of physical reality be considered complete?" Phys. Rev. **47**, 777 (1935).

[2] E. Schrödinger, "Discussion of Probability Relations between Separated Systems," Math. Proc. Cambridge **31**, 555 (1935).

[3] J. S. Bell, "On the problem of hidden variables in quantum mechanics," Rev. of Mod. Phys. **38**, 447 (1966).

[4] J. F. Clauser, M. A. Horne, A. Shimony, and R. A. Holt, "Proposed experiment to test local hidden-variable theories," Phys. Rev. Lett. **23**, 880 (1969).

[5] J. G. Rarity and P. R. Tapster, "Experimental violation of bell's inequality based on phase and momentum," Phys. Rev. Lett. **64**, 2495 (1990).

[6] S. J. Freedman and J. F. Clauser, "Experimental Test of Local Hidden-Variable Theories," Phys. Rev. Lett. **28**, 938 (1972).

[7] A. Aspect, P. Grangier, and G. Roger, "Experimental Realization of Einstein-Podolsky-Rosen-Bohm *Gedankenexperiment* : A New Violation of Bell's Inequalities," Phys. Rev. Lett. **49**, 91 (1982).

[8] O. Benson, C. Santori, M. Pelton, and Y. Yamamoto, "Regulated and Entangled Photons from a Single Quantum Dot," Phys. Rev. Lett. **84**, 2513 (2000).

[9] N. Akopian, N. H. Lindner, E. Poem, Y. Berlatzky, J. Avron, D. Gershoni, B. D. Gerardot, and P. M. Petroff, "Entangled Photon Pairs from Semiconductor Quantum Dots," Phys. Rev. Lett. **96**, 130501 (2006).

[10] S. P. Walborn, A. N. de Oliveira, R. S. Thebaldi, and C. H. Monken, "Entanglement and conservation of orbital angular momentum in spontaneous parametric down-conversion," Phys. Rev. A **69**, 023811 (2004).

[11] G. Molina-Terriza, J. P. Torres, and L. Torner, "Twisted photons," Nature Physics **3**, 305 (2007).

[12] D. Bouwmeester, J.-W. Pan, K. Mattle, M. Eibl, H. Weinfurter, and A. Zeilinger, "Experimental quantum teleportation," Nature **390**, 575 (1997).

[13] P. G. Kwiat, E. Waks, A. G. White, I. Appelbaum, and P. H. Eberhard, "Ultra-bright source of polarization-entangled photons," Phys. Rev. A **60**, 773 (1999).

[14] Z. Ou, C. Hong, and L. Mandel, "Violations of locality in correlation measurements with a beam splitter," Phys. Lett A **122**, 11 (1987).

[15] N. Matsuda, H. Le Jeannic, H. Fukuda, T. Tsuchizawa, W. J. Munro, K. Shimizu, K. Yamada, Y. Tokura, and H. Takesue, "A monolithically integrated polarization entangled photon pair source on a silicon chip," Scientific reports **2** (2012).

[16] M. Savanier, A. Andronico, A. Lemaître, E. Galopin, C. Manquest, I. Favero, S. Ducci, and G. Leo, "Large second-harmonic generation at 1.55?μmin oxidized algaas waveguides," Opt. Lett. **36**, 2955 (2011).

[17] R. Horn, P. Abolghasem, B. J. Bijlani, D. Kang, A. S. Helmy, and G. Weihs, "Monolithic source of photon pairs," Phys. Rev. Lett. **108**, 153605 (2012).

[18] M. F. Saleh, B. E. A. Saleh, and M. C. Teich, "Modal, spectral, and polarization entanglement in guided-wave parametric down-conversion," Phys. Rev. A **79**, 053842 (2009).

[19] J. Lugani, S. Ghosh, and K. Thyagarajan, "Generation of modal- and path-entangled photons using a domain-engineered integrated optical waveguide device," Phys. Rev. A **83**, 062333 (2011).

[20] C. K. Law, I. A. Walmsley, and J. H. Eberly, "Continuous Frequency Entanglement: Effective Finite Hilbert Space and Entropy Control," Phys. Rev. Lett. **84**, 5304 (2000).

[21] C. K. Law and J. H. Eberly, "Analysis and Interpretation of High Transverse Entanglement in Optical Parametric Down Conversion," Phys. Rev. Lett. **92**, 127903 (2004).

[22] R. Horodecki, P. Horodecki, M. Horodecki, and K. Horodecki, "Quantum entanglement," Rev. Mod. Phys. **81**, 865 (2009).

[23] C. H. Bennett and S. J. Wiesner, "Communication via one-and two-particle operators on Einstein-Podolsky-Rosen states," Phys. Rev. Let. **69**, 2881 (1992).

[24] C. H. Bennett, G. Brassard, C. Crépeau, R. Jozsa, A. Peres, and W. K. Wootters, "Teleporting an unknown quantum state via dual classical and Einstein-Podolsky-Rosen channels," Phys. Rev. Let. **70**, 1895 (1993).

[25] A. K. Ekert, "Quantum cryptography based on Bell's theorem," Phys. Rev. Let. **67**, 661 (1991).

[26] W. P. Schleich and H. Walther, *Elements of quantum information* (Wiley-VCH, 2007).

[27] M. A. Nielsen and I. L. Chuang, *Quantum computation and quantum information* (Cambridge university press, 2010).

[28] D. Deutsch, "Quantum theory, the Church-Turing principle and the universal quantum computer," P. Roy. Soc. Lond. A. Mat. **400**, 97 (1985).

[29] P. W. Shor, "Algorithms for quantum computation: discrete logarithms and factoring," in "Foundations of Computer Science, 1994 Proceedings., 35th Annual Symposium on," (IEEE, 1994), p. 124.

[30] L. K. Grover, "A fast quantum mechanical algorithm for database search," in "Proceedings of the twenty-eighth annual ACM symposium on Theory of computing," (ACM, 1996), p. 212.

[31] V. Giovannetti, S. Lloyd, and L. Maccone, "Quantum metrology," Phys. Rev. Let. **96**, 10401 (2006).

[32] M. I. Kolobov, *Quantum imaging* (Springer, 2007).

[33] S. F. Huelga, C. Macchiavello, T. Pellizzari, A. K. Ekert, M. B. Plenio, and J. I. Cirac, "Improvement of frequency standards with quantum entanglement," Phys. Rev. Let. **79**, 3865 (1997).

[34] M. B. Nasr, B. E. A. Saleh, A. V. Sergienko, and M. C. Teich, "Demonstration of dispersion-canceled quantum-optical coherence tomography," Phys. Rev. Let. **91**, 83601 (2003).

[35] K. A. O'Donnell, "Observations of dispersion cancellation of entangled photon pairs," Phys. Rev. Lett. **106**, 063601 (2011).

[36] J. P. Dowling, "Quantum optical metrology – the lowdown on high-N00N states," Contemp. Phys. **49**, 125 (2008).

[37] N. Bloembergen, "Conservation laws in nonlinear optics," J. Opt. Soc. Am. **70**, 1429 (1980).

[38] R. W. Boyd, *Nonlinear optics* (Academic press, 2002).

[39] Y.-R. Shen, *The principles of nonlinear optics*, vol. 1 (New York, Wiley-Interscience, 1984).

[40] G. G. Gurzadian, V. G. Dmitriev, and D. N. Nikogosian, *Handbook of nonlinear optical crystals* (Springer-Verlag, Berlin ; New York :, 1991).

[41] W. Greiner, *Quantum mechanics: special chapters*, vol. 4 (Springer Verlag, 1998).

[42] M. O. Scully and M. S. Zubairy, *Quantum Optics* (Cambridge University Press; 1 edition, 1997).

[43] W. H. Louisell, A. Yariv, and A. E. Siegman, "Quantum Fluctuations and Noise in Parametric Processes. I." Phys. Rev. **124**, 1646 (1961).

[44] J. P. Gordon, W. H. Louisell, and L. R. Walker, "Quantum Fluctuations and Noise in Parametric Processes. II," Phys. Rev. **129**, 481 (1963).

[45] D. C. Burnham and D. L. Weinberg, "Observation of Simultaneity in Parametric Production of Optical Photon Pairs," Phys. Rev. Lett. **25**, 84 (1970).

[46] C. K. Hong and L. Mandel, "Theory of parametric frequency down conversion of light," Phys. Rev. A **31**, 2409 (1985).

[47] B. E. A. Saleh and M. C. Teich, *Fundamentals of Photonics* (Wiley, New York, 1991).

[48] J. Perina, *Quantum statistics of linear and nonlinear optical phenomena* (Kluwer Academic Pub, 1991).

[49] W. Wasilewski, A. I. Lvovsky, K. Banaszek, and C. Radzewicz, "Pulsed squeezed light: Simultaneous squeezing of multiple modes," Phys. Rev. A **73**, 063819 (2006).

[50] C. K. Hong, Z. Y. Ou, and L. Mandel, "Measurement of subpicosecond time intervals between two photons by interference," Phys. Rev. Lett. **59**, 2044 (1987).

[51] L. Mandel and E. Wolf, *Optical coherence and quantum optics* (Cambridge university press, 1995).

[52] M. H. Rubin, D. N. Klyshko, Y. H. Shih, and A. V. Sergienko, "Theory of two-photon entanglement in type-ii optical parametric down-conversion," Phys. Rev. A **50**, 5122 (1994).

[53] A. S. Helmy, B. Bijlani, and P. Abolghasem, "Phase matching in monolithic Bragg reflection waveguides," Opt. Lett. **32**, 2399 (2007).

[54] P. Abolghasem, M. Hendrych, X. Shi, J. P. Torres, and A. S. Helmy, "Bandwidth control of paired photons generated in monolithic bragg reflection waveguides," Opt. Lett. **34**, 2000 (2009).

[55] A. Fiore, V. Berger, E. Rosencher, P. Bravetti, and J. Nagle, "Phase matching using an isotropic nonlinear optical material," Nature **391**, 463 (1998).

[56] J. Armstrong, N. Bloembergen, J. Ducuing, and P. Pershan, "Interactions between light waves in a nonlinear dielectric," Phys. Rev. **127**, 1918 (1962).

[57] M. M. Fejer, G. Magel, D. H. Jundt, and R. L. Byer, "Quasi-phase-matched second harmonic generation: tuning and tolerances," IEEE J. Quant. Electron. **28**, 2631 (1992).

[58] S. Yoo, R. Bhat, C. Caneau, and M. Koza, "Quasi-phase-matched second-harmonic generation in algaas waveguides with periodic domain inversion achieved by wafer-bonding," App. Phys. Let. **66**, 3410 (1995).

[59] T. Skauli, K. L. Vodopyanov, T. J. Pinguet, A. Schober, O. Levi, L. A. Eyres, M. M. Fejer, J. S. Harris, B. Gerard, L. Becouarn, E. Lallier, and G. Arisholm, "Measurement of the nonlinear coefficient of orientation-patterned gaas and demonstration of highly efficient second-harmonic generation," Opt. Lett. **27**, 628 (2002).

[60] K. L. Vodopyanov, O. Levi, P. S. Kuo, T. J. Pinguet, J. S. Harris, M. M. Fejer, B. Gerard, L. Becouarn, and E. Lallier, "Optical parametric oscillation in quasi-phase-matched GaAs," Opt. Lett. **29**, 1912 (2004).

[61] M. Baudrier-Raybaut, R. Haidar, P. Kupecek, P. Lemasson, and E. Rosencher, "Random quasi-phase-matching in bulk polycrystalline isotropic nonlinear materials," Nature **432**, 374 (2004).

[62] S. Kawai, T. Ogawa, H. S. Lee, R. C. DeMattei, and R. S. Feigelson, "Second-harmonic generation from needlelike ferroelectric domains in $Sr_{0.6}Ba_{0.4}Nd_2O_6$ single crystals," App. Phys. Let. **73**, 768 (1998).

[63] R. Fischer, S. M. Saltiel, D. N. Neshev, W. Krolikowski, and Y. S. Kivshar, "Broadband femtosecond frequency doubling in random media," App. Phys. Let. **89**, 191105 (2006).

[64] E. Y. Morozov and A. S. Chirkin, "Consecutive Parametric Interactions of Light Waves with Nonmultiple Frequencies in Crystals with Irregular Poled Structure," J. Russ. Laser Res. **25**, 299 (2004).

[65] X. Vidal and J. Martorell, "Generation of Light in Media with a Random Distribution of Nonlinear Domains," Phys. Rev. Lett. **97** (2006).

[66] A. S. Aleksandrovsky, A. M. Vyunishev, I. E. Shakhura, A. I. Zaitsev, and A. V. Zamkov, "Random quasi-phase-matching in a nonlinear photonic crystal structure of strontium tetraborate," Phys. Rev. A **78** (2008).

[67] M. Centini, D. Felbacq, D. S. Wiersma, C. Sibilia, M. Scalora, and M. Bertolotti, "Resonant second harmonic generation in random dielectric structures," J. Eur. Opt. Soc. Rapid Publ. **1**, 06021 (2006).

[68] G. K. Kitaeva, "Frequency conversion in aperiodic quasi-phase-matched structures," Phys. Rev. A **76**, 043841 (2007).

[69] J. S. Pelc, C. Langrock, Q. Zhang, and M. M. Fejer, "Influence of domain disorder on parametric noise in quasi-phase-matched quantum frequency converters," Opt. Lett. **35**, 2804 (2010).

[70] R. Fischer, S. M. Saltiel, D. N. Neshev, W. Krolikowski, and Y. S. Kivshar, "Transverse second-harmonic generation from disordered nonlinear crystals," Cent. Eur. J. Phys. **6**, 569 (2008).

[71] J. Peřina, M. Centini, C. Sibilia, and M. Bertolotti, "Photon-pair generation in random nonlinear layered structures," Phys. Rev. A **80**, 033844 (2009).

[72] M. Yamada, N. Nada, M. Saitoh, and K. Watanabe, "First-order quasi-phase matched $LiNbO_3$ waveguide periodically poled by applying an external field for efficient blue second-harmonic generation," App. Phys. Let. **62**, 435 (1993).

[73] J.-P. Meyn, C. Laue, R. Knappe, R. Wallenstein, and M. Fejer, "Fabrication of periodically poled lithium tantalate for UV generation with diode lasers," App. Phys. B **73**, 111 (2001).

[74] M. Peltz, U. Bäder, A. Borsutzky, R. Wallenstein, J. Hellström, H. Karlsson, V. Pasiskevicius, and F. Laurell, "Optical parametric oscillators for high pulse energy and high average power operation based on large aperture periodically poled ktp and rta," App. Phys. B **73**, 663 (2001).

[75] S. Carrasco, J. P. Torres, L. Torner, A. Sergienko, B. E. A. Saleh, and M. C. Teich, "Enhancing the axial resolution of quantum optical coherence tomographyby chirped quasi-phase matching," Opt. Lett. **29**, 2429 (2004).

[76] M. B. Nasr, S. Carrasco, B. E. A. Saleh, A. V. Sergienko, M. C. Teich, J. P. Torres, L. Torner, D. S. Hum, and M. M. Fejer, "Ultrabroadband Biphotons Generated via Chirped Quasi-Phase-Matched Optical Parametric Down-Conversion," Phys. Rev. Lett. p. 183601 (2008).

[77] S. E. Harris, "Chirp and Compress: Toward Single-Cycle Biphotons," Phys. Rev. Lett. **98**, 063602 (2007).

[78] A. M. Steinberg, P. G. Kwiat, and R. Y. Chiao, "Dispersion cancellation in a measurement of the single-photon propagation velocity in glass," Phys. Rev. Lett. **68**, 2421 (1992).

[79] J. Peřina Jr., A. V. Sergienko, B. M. Jost, B. E. A. Saleh, and M. C. Teich, "Dispersion in femtosecond entangled two-photon interference," Phys. Rev. A **59**, 2359 (1999).

[80] B. Dayan, Y. Bromberg, I. Afek, and Y. Silberberg, "Spectral polarization and spectral phase control of time-energy entangled photons," Phys. Rev. A **75**, 043804 (2007).

[81] G. Brida, M. V. Chekhova, I. P. Degiovanni, M. Genovese, G. K. Kitaeva, A. Meda, and O. A. Shumilkina, "Chirped biphotons and their compression in optical fibers," Phys. Rev. Lett. **103**, 193602 (2009).

[82] S. Sensarn, G. Y. Yin, and S. E. Harris, "Generation and Compression of Chirped Biphotons," Phys. Rev. Lett. **104**, 253602 (2010).

[83] J. Peřina Jr., M. Centini, C. Sibilia, M. Bertolotti, and M. Scalora, "Properties of entangled photon pairs generated in one-dimensional nonlinear photonic-band-gap structures," Phys. Rev. A **73**, 033823 (2006).

[84] M. Hamar, J. Peřina Jr., O. Haderka, and V. Michálek, "Chirp and Compress: Toward Single-Cycle Biphotons," Phys. Rev. A **81**, 043827 (2010).